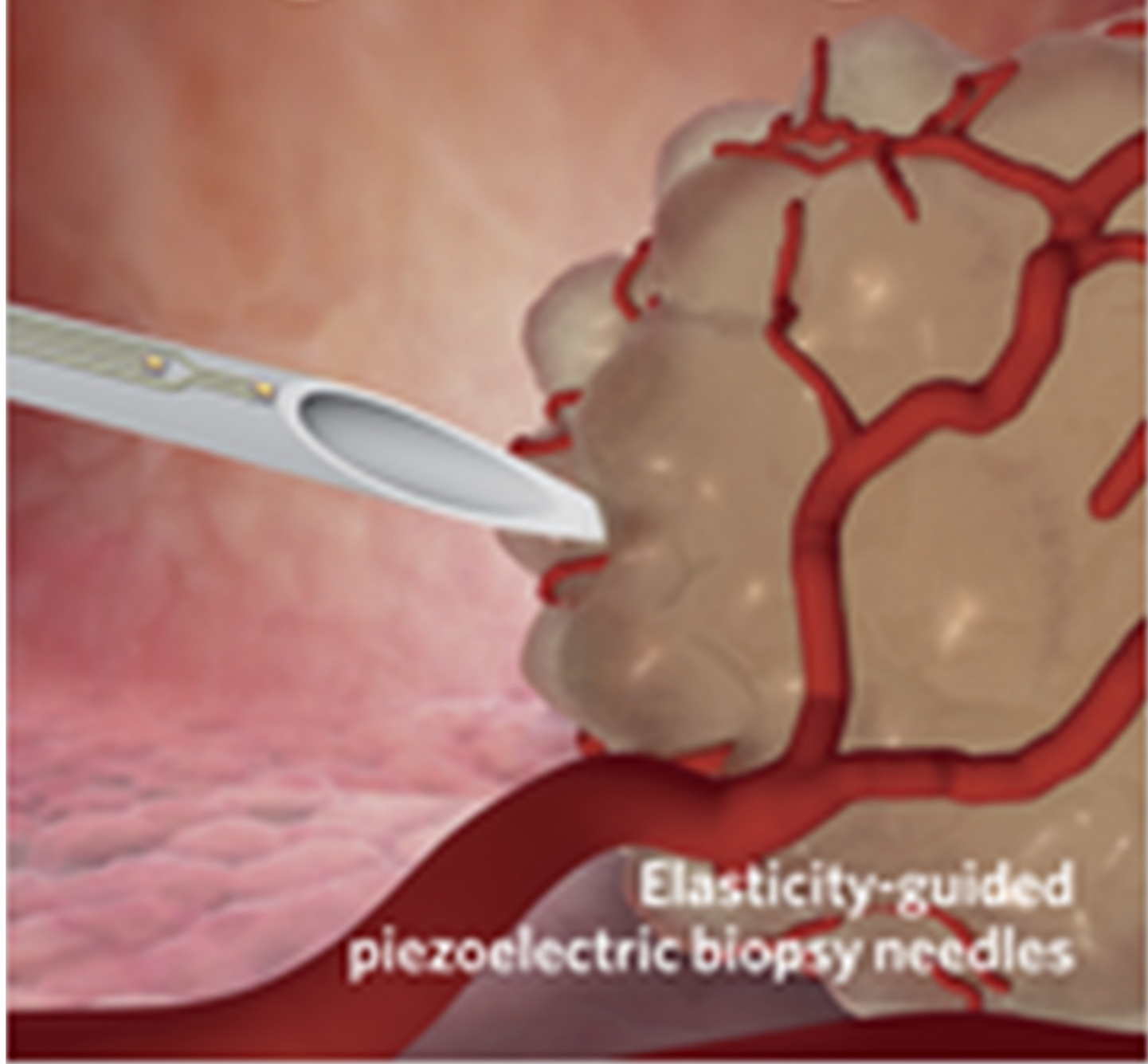


nature biomedical engineering



Elasticity-guided
piezoelectric biopsy needles

Needle-shaped ultrathin piezoelectric microsystem for guided tissue targeting via mechanical sensing

Xinge Yu^{1,2,19}, Heling Wang^{3,4,5,19}, Xin Ning^{2,19}, Rujie Sun^{2,6}, Hassan Albadawi⁷, Marcela Salomao⁸, Alvin C. Silva⁹, Yang Yu^{2,10}, Limei Tian^{2,11}, Ahyeon Koh¹², Chan Mi Lee², Aditya Chempakasseril², Peilin Tian², Matt Pharr¹³, Jianghong Yuan^{3,4,5,14}, Yonggang Huang^{3,4,5*}, Rahmi Oklu^{10,7*} and John A. Rogers^{1,2,5,15,16,17,18*}

Needles for percutaneous biopsies of tumour tissue can be guided by ultrasound or computed tomography. However, despite best imaging practices and operator experience, high rates of inadequate tissue sampling, especially for small lesions, are common. Here, we introduce a needle-shaped ultrathin piezoelectric microsystem that can be injected or mounted directly onto conventional biopsy needles and used to distinguish abnormal tissue during the capture of biopsy samples, through quantitative real-time measurements of variations in tissue modulus. Using well-characterized synthetic soft materials, explanted tissues and animal models, we establish experimentally and theoretically the fundamental operating principles of the microsystem, as well as key considerations in materials choices and device designs. Through systematic tests on human livers with cancerous lesions, we demonstrate that the piezoelectric microsystem provides quantitative agreement with magnetic resonance elastography, the clinical gold standard for the measurement of tissue modulus. The piezoelectric microsystem provides a foundation for the design of tools for the rapid, modulus-based characterization of tissues.

Accurately targeting a tumour site during needle-based biopsy procedures is critical for diagnosis and for personalized strategies in cancer treatment, where the biopsy tissue is essential for genomic screening¹. Approximately one in five biopsy samples are not viable for analysis owing to the insufficient number of malignant cells that often results from imprecise image-guided targeting of the biopsy needle into the tumour². Repeating these invasive biopsy procedures increases the potential for complications for the patient, including tumour seeding; therefore, success following the initial biopsy is crucial^{3,4}. Even the much anticipated national pan-cancer Molecular Analysis for Therapy Choice (MATCH) clinical trial, which aimed to use genomic analysis to advance precision medicine, suffered from major sample-quality issues impacting 94 of the 739 cases during an interim analysis; 127 samples could not be analysed for reasons that included insufficient tumour or tissue to allow for genomic analysis^{5,6}.

Erroneous targeting of tumour tissue resulting in minimal or no malignant cells in the biopsy specimens can lead to misdiagnosis and delayed care. Ultrasound and computed tomography are

helpful in guiding needles to the tumour tissue^{6,7}; however, the accuracy and utility of these imaging tools can be limited, especially when lesions are small, are affected by motion (especially during respiration), cannot be seen without contrast agents, or are mobile, such as lymph nodes. Because of inherent risks to renal function, intravenous contrast is often not used during biopsy procedures; thus, percutaneous placement of the needle, especially with computed tomography guidance, relies on the ability of the operator to use adjacent landmarks, such as bony structures, for guidance. Additional risks due to radiation exposure to the patient and operator from prolonged computed tomography fluoroscopy use also impact the success of guidance. As a result, despite best imaging practices and operator experience, high rates of false negatives and inadequate tissue sampling of lesions <1 mm in the lungs and <3 cm in the abdomen are common⁸.

Recent reports show that disease states, ranging from inflammation to fibrosis to cancer, alter the mechanical properties of tissues, suggesting a potential for the use of targeting biopsy needles^{9–11}. Specifically, measurements of the mechanical properties of soft

¹Simpson Querrey Center and Feinberg School of Medicine, Center for Bio-Integrated Electronics, Northwestern University, Evanston, IL, USA. ²Department of Materials Science and Engineering, Frederick Seitz Materials Research Laboratory, University of Illinois at Urbana-Champaign, Urbana, IL, USA.

³Department of Civil and Environmental Engineering, Northwestern University, Evanston, IL, USA. ⁴Department of Mechanical Engineering, Northwestern University, Evanston, IL, USA. ⁵Department of Materials Science and Engineering, Northwestern University, Evanston, IL, USA. ⁶Advanced Composites Centre for Innovation and Science, University of Bristol, Bristol, UK. ⁷Division of Vascular and Interventional Radiology, Minimally Invasive Therapeutics Laboratory, Mayo Clinic, Phoenix, AZ, USA. ⁸Department of Pathology, Mayo Clinic, Phoenix, AZ, USA. ⁹Division of Abdominal Imaging, Mayo Clinic, Phoenix, AZ, USA. ¹⁰Department of Materials Science and Engineering, Tsinghua University, Beijing, China. ¹¹Beckman Institute for Advanced Science and Technology, University of Illinois at Urbana-Champaign, Urbana, IL, USA. ¹²Department of Biomedical Engineering, Binghamton University, Binghamton, NY, USA. ¹³Department of Mechanical Engineering, Texas A&M University, College Station, TX, USA. ¹⁴Center for Mechanics and Materials, and Applied Mechanics Laboratory, Department of Engineering Mechanics, Tsinghua University, Beijing, China. ¹⁵Department of Biomedical Engineering, Northwestern University, Evanston, IL, USA. ¹⁶Department of Neurological Surgery, Northwestern University, Evanston, IL, USA. ¹⁷Department of Chemistry, Northwestern University, Evanston, IL, USA. ¹⁸Department of Electrical Engineering and Computer Science, Northwestern University, Evanston, IL, USA. ¹⁹These authors contributed equally: Xinge Yu, Heling Wang and Xin Ning. *e-mail: y-huang@northwestern.edu; oklu.rahmi@mayo.edu; jrogers@northwestern.edu

tissues, particularly the elastic modulus, can be used to distinguish healthy and diseased tissues such as in the liver, kidney, lung and brain^{12–16}. For example, in the liver, tumours exhibit abnormally high stiffness and densities compared with surrounding soft tissue¹⁰. As normal tissue becomes afflicted with disease, such as chronic inflammation or malignancy, the local modulus changes significantly, suggesting that this mechanical property could be used as a marker of pathology, specifically neoplasms. Thus, minimally invasive measurements of modulus may allow the detection of tumours with high accuracy¹⁷. Existing characterization methods rely on bulk measurements of displacement (that is, strain) as a function of applied force (that is, stress) delivered with instruments that apply vacuum suction¹⁸, tools that impart compressive forces¹⁹ or fine tips that induce small-scale indentations²⁰, all typically ex vivo. The associated instruments with these methods often involve large equipment, thereby precluding their use in the direct evaluation of tissues in patients during surgical procedures²¹. Non-invasive measurements for estimating tissue lesions are possible with acoustic methods, such as ultrasound⁶ and acoustic radiation force impulse imaging²¹. However, magnetic resonance elastography (MRE) allows non-invasive measurements of modulus in which (1) external excitation leads to shear waves inside the tissue, (2) spatio-temporal information is yielded on the propagation of these waves and (3) data processing produces colour-coded quantitative maps of tissue stiffness²². Recent reports describe the use of MRE to identify and localize diseased tissue, such as in the liver for fibrosis²³, kidneys²⁴ and breasts²⁵ for tumours, and spleen²³ and lung²⁶ for quantitating stiffness. These results clearly demonstrate that mechanical properties can be used clinically to distinguish tissue types and advance the assessment of tissue. Abnormalities detected by MRE often trigger additional exams, such as computed-tomography-guided biopsies for diagnosis and genetic analysis^{27,28}.

Here, we present advances in materials and device engineering that have the potential to allow accurate targeting of tumour tissue. These adapt and extend recently reported technologies for characterizing the mechanical properties of the skin to needle-based systems for tissue targeting in the context of percutaneous biopsies²⁹. Embodiments of our technology include both free-standing, flexible penetrating pins and thin laminates on standard instruments for performing biopsies. Extensive ex vivo and in vivo evaluations of various normal and diseased tissues, including human livers, illustrate the measurement capabilities, with quantitative comparisons to clinical standards such as MRE. These studies establish the foundations for minimally invasive sensors for improving tissue targeting, where Young's modulus serves as the basis for guiding accurate specimen collection for histological and genetic testing.

Results and discussion

Materials, designs and fabrication procedures for needle-based modulus probes. Figure 1a shows schematic illustrations of two kinds of modulus-sensing probe. In both, two separate micro-components (lateral dimensions of 200 μm × 140 μm, separated by 1 mm) constructed with the piezoelectric material lead zirconate titanate (PZT) provide mechanical actuation (distant from the tip) and sensing (near the tip). The modulus of the adjacent contacting tissue can be extracted by interpreting data that follow from applying voltage to the mechanical actuator and measuring the induced voltage of the sensor. These active elements consist of patterned multilayer stacks of PZT (500 nm) between bottom (Ti/Pt, 5 nm/200 nm) and top (Cr/Au, 10 nm/200 nm) electrodes (Supplementary Figs. 1 and 2), with an overcoat of polyimide (PI) for encapsulation (inset of Fig. 1a and Supplementary Fig. 4). The first embodiment (device 1) adopts a free-standing design in the shape of a penetrating pin, built on a thin, flexible substrate of 75-μm-thick PI (Supplementary Figs. 3 and 4)³⁰. A magnified view is shown in Fig. 1b. The sharp tip geometry and narrow width

(0.5 mm, with 4 mm length; Supplementary Fig. 5) allow penetration through soft tissues for injection into targeted regions^{31,32}. Previous studies of the constituent materials reveal no evidence of toxicity²⁹. The electrodes for the sensors and actuators interface to input/output channels through photolithographically defined electrical interconnects (Au, 200 nm thick).

The second embodiment (device 2) uses a conventional steel biopsy needle as a platform to enable penetration of skin, fascia and solid organs and positioning within a lesion for the assessment of organ pathology, diagnosis and/or treatment. The main difference compared with the design of device 1 is the use of an ultra-thin (3 μm) sheet of PI (1.5 mm width, 4.5 mm length) as a substrate to allow sharp bending for conformal lamination onto the tip end region of the biopsy needle (Fig. 1c). A thin (50 μm) interlayer of polydimethylsiloxane (PDMS) (modulus of ~100 kPa) lies between the bottom side of the PI and the surface of the needle, as a means to mechanically decouple the device from the steel needle, for reasons described later. Images of both devices are shown in Fig. 1d–f and Supplementary Fig. 6.

Finite element analysis (FEA) indicates that for a given actuation voltage, the sensor voltage relates to the modulus of the tissue through mechanical coupling among the actuator, substrate, tissue and sensor. With the device inserted into—and firmly in contact with—the tissue, application of a voltage leads to mechanical strain in the actuator via the piezoelectric effect, and a slight resultant bending of the needle substrate. The associated deformation of the surrounding tissue creates strain in the sensor. Through the inverse piezoelectric effect, this strain produces a measurable voltage; the magnitude of the strain, and therefore the voltage, depends on the tissue modulus. Figure 2a shows the model for FEA, while Fig. 2b illustrates the deformations in the device and surrounding tissue. The results in Fig. 2c,d indicate that strains induced in the tissue and devices (actuator, PI or PDMS-coated steel needle substrate and sensor) are very small (<0.1%) for applied voltages in a practical range (up to several volts).

Fundamental studies of operational principles. The FEA results of Supplementary Fig. 7a reveal the dependence of the sensor voltage on tissue modulus. Specifically, the voltage increases by one order of magnitude when the tissue modulus increases from 1 kPa to 100 kPa. The voltage then decreases as the tissue modulus increases beyond this upper value. This non-monotonic relationship can be understood qualitatively as a balance of two considerations: (1) in the regime of low modulus, the actuator and substrate deform freely, with highly localized responses that lead to small strains in the sensor and correspondingly small sensor voltages; and (2) in the regime of high modulus, mechanical loading associated with the surrounding tissue limits the deformation of the actuator and the substrate, again leading to small sensor voltages. The sensor voltage reaches a maximum between these two limiting regimes at ~100 kPa in Supplementary Fig. 7b.

A scaling law that relates the tissue modulus E_{tissue} and sensor voltage V_{sensor} can be established for values of the tissue modulus between 1 kPa and 1,000 kPa, as (see Supplementary Information for details)

$$\frac{V_{\text{sensor}}}{V_{\text{actuator}}} = \frac{e_{31}^2 A_{\text{PZT}} h_{\text{PZT}}}{k_{33} E_{\text{PI}} h_{\text{PI}} d^2} G \left(\frac{E_{\text{tissue}} d^3}{E_{\text{PI}} h_{\text{PI}}^3} \right) \quad (1)$$

where V_{actuator} is the actuator voltage and the other parameters and variables can be grouped into (1) material properties: the piezoelectric coefficient e_{31} and dielectric coefficient k_{33} of the actuator and sensor made of PZT, and the modulus E_{PI} of the needle substrate made of PI; and (2) geometric parameters: thickness h_{PZT} and area A_{PZT} perpendicular to the polarization direction of the actuator and

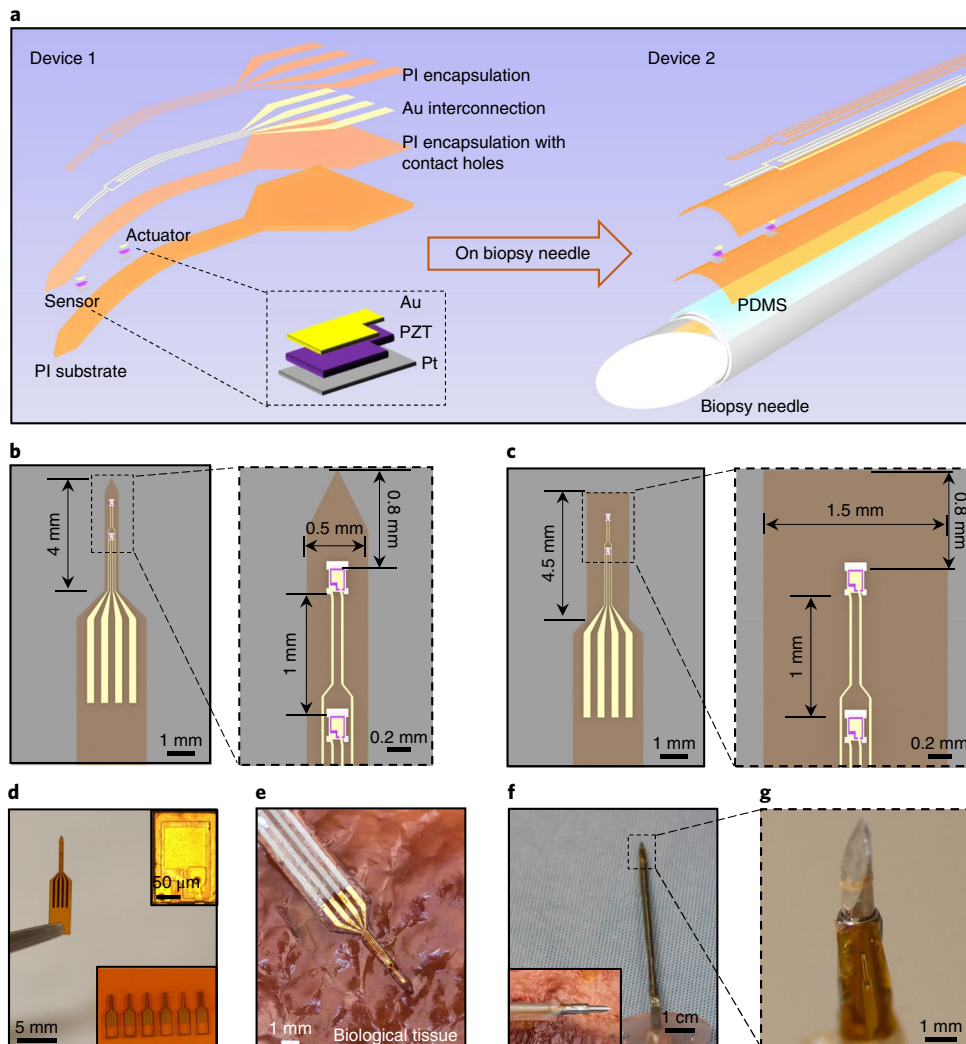


Fig. 1 | Tissue modulus probes based on ultrathin PZT actuators and sensors. **a**, Exploded-view schematic illustrations of device 1 (free standing) and device 2 (integrated on a biopsy needle). PZT, lead zirconate titanate; PDMS, polydimethylsiloxane; PI, polyimide. **b,c**, Schematic illustrations with key dimensions of the sensor and actuator regions for device 1 (**b**) and device 2 (**c**). **d**, Optical images of device 1. The insets show an array of devices (bottom) and a magnified view of a sensor/actuator pair (top). **e**, Image of device 1 placed on a biological tissue. **f**, Optical images of device 2. The inset shows an image of device 2 on a biological tissue. **g**, Magnified view of the sensor and actuator regions on the biopsy needle substrate.

sensor, thickness h_{PI} of the needle substrate, and spacing d between the actuator and the sensor. The function G depends on the tissue modulus and spacing via $E_{\text{tissue}}d^3$ normalized by the bending stiffness of the needle substrate, as in Supplementary Fig. 8. For $h_{\text{PZT}} \ll h_{\text{PI}} \ll w_{\text{PI}}$, L_{PI} (where w_{PI} is the width of the needle substrate and L_{PI} is the length of the needle substrate) and $h_{\text{PZT}} \ll L_{\text{PZT}}$, $w_{\text{PZT}} \ll d \ll w_{\text{PI}}$, L_{PI} (where L_{PZT} is the length of the actuator and sensor, and w_{PZT} is the width of the actuator and sensor), equation (1) is consistent with FEA, as shown in Supplementary Fig. 8.

This scaling law also gives the critical tissue modulus E_{tissue}^* below which the relationship between sensor voltage and tissue modulus is monotonic as (for example, ~100 kPa in Supplementary Fig. 7)

$$E_{\text{tissue}}^* = 0.2 \frac{E_{\text{PI}} h_{\text{PI}}^3}{d^3} \quad (2)$$

which can be controlled by changing the modulus of the needle substrate, the thickness or the spacing between the actuator and sensor, as illustrated in Supplementary Fig. 9. Simulations indicate

that the sensor can measure samples with dimensions as small as $1 \text{ mm} \times 1 \text{ mm} \times 1.5 \text{ mm}$ (length \times width \times thickness), as shown in Supplementary Fig. 10. Insights from this theoretical treatment establish the foundations for both design guidelines and analysis approaches.

In practical modes of operation, alternating current voltages drive the actuator, while lock-in techniques extract corresponding alternating current voltages from the sensor, typically in a frequency range of 1~100 Hz. The data-recording system includes a lock-in amplifier (SR830, Stanford Research Systems), a bio-amplifier (ADI Instruments) and a computer for determining the amplitude of the voltage response from the sensors²⁹. Tests on samples of PDMS with Young's moduli similar to those of biological tissues validate this type of measurement³³. Here, dynamic mechanical analysis (DMA) of the same samples provides comparative data on the storage and loss moduli. As expected from FEA predictions that use the moduli determined by DMA, the sensor voltage is independent of the actuation frequency from 1 to ~100 Hz (Fig. 2e). As a result, viscoelastic effects can be neglected; we confirmed that they can also be neglected for the biological samples, as is shown in Fig. 2f.

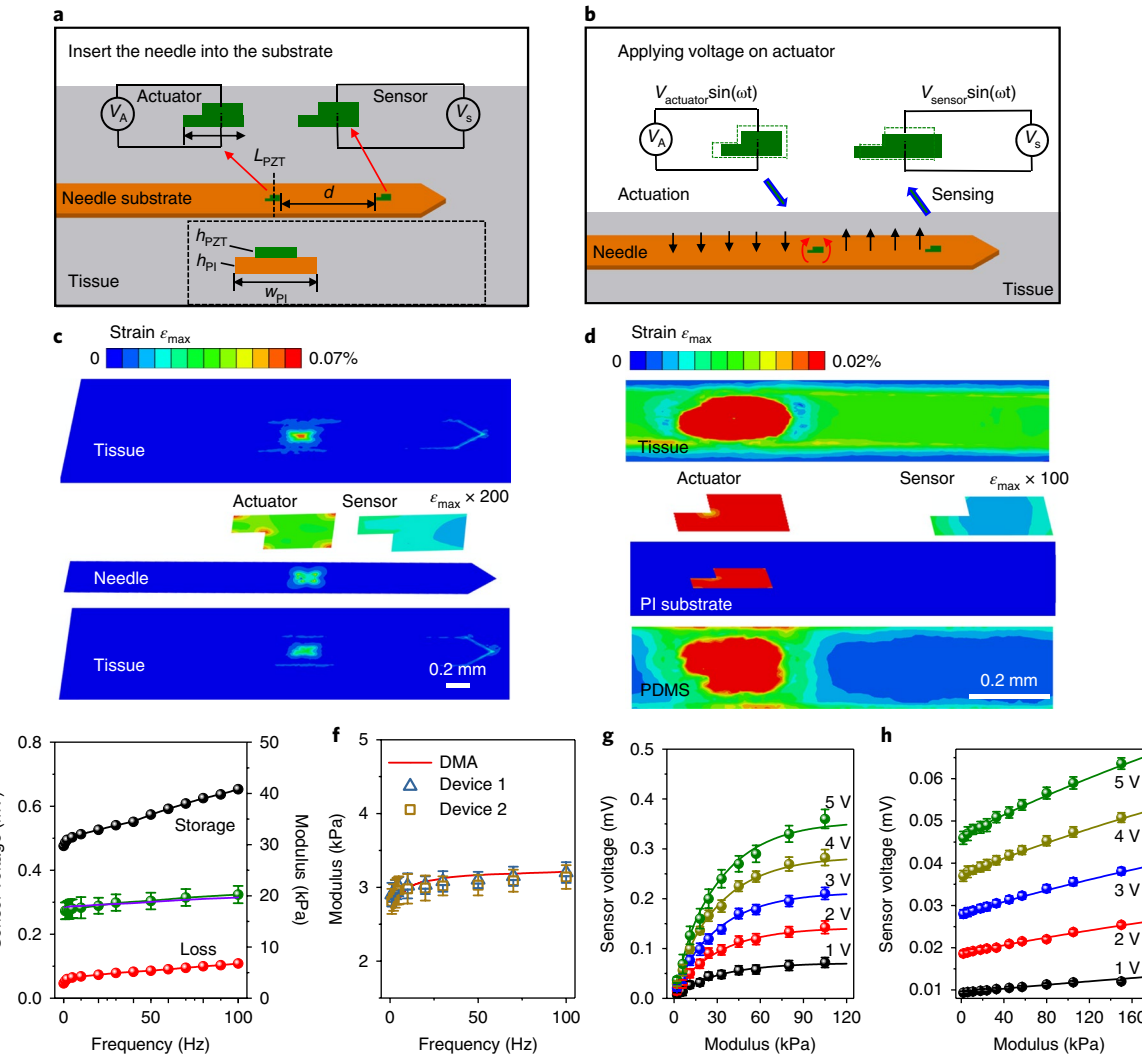


Fig. 2 | Fundamental studies of device operation. **a,b**, Working principles of a modulus probe injected into a tissue sample. **c,d**, Distribution of maximum principal strain ϵ_{max} in the tissue, needle, actuator and sensor (actuator voltage 5 V, tissue modulus 100 kPa) for device 1 (**c**) and device 2 (**d**). **e**, Output voltage of the sensor in device 1 as a function of the actuation frequency, and the dynamic mechanics analysis results from the measured sample. **f**, Modulus of fresh pig liver measured by DMA and devices 1 and 2. **g,h**, Output voltage of a sensor as a function of the modulus of the samples tested, for device 1 (**g**) and device 2 (**h**). In **e–h**, the symbols and lines correspond to experimental and theoretical results, respectively. Error bars correspond to calculated standard error deviation for at least 20 samples.

The effects of inertia are negligible owing to the low operating frequencies (below 100 Hz), such that harmonic vibrations can be considered as quasi-static. For consistency, we used a frequency of 100 Hz in the studies described next.

Quantitative calibration and measurement of artificial tissue samples. Evaluation of a set of agarose gel (Sigma-Aldrich) samples formulated to yield a range of Young's modulus values that span those of inner body soft organ tissues^{10,34,35} confirmed the relationships and calibration procedures outlined in the previous section, as shown in Supplementary Fig. 11. Supplementary Fig. 12 presents the actuator voltage (peak value) in device 1 as a function of sensor voltage for artificial tissues with various modulus values. The sensor voltages increase linearly with actuator voltage for each sample (moduli between 1 and 105 kPa). As a function of modulus, the sensor voltage varies in a fashion (Fig. 2g) consistent with FEA results and with previously described qualitative considerations. DMA measurements, FEA simulations and data from the needle devices precisely and completely define the relationship between modulus

and sensor voltages, for given actuator voltage, as shown in Fig. 2g and Supplementary Fig. 12.

Similar studies define the operation of the biopsy needle embodiment (device 2), as shown in Supplementary Figs. 13 and 14. Here, a monotonic linear relationship exists between the sensor voltage and tissue modulus (Supplementary Fig. 15), up to values of 1 MPa, consistent with replacement of the quantity $E_{PI} \times h_{PI}^3$ with K —an effective stiffness that is significantly larger than $E_{PI} \times h_{PI}^3$ due to the influence of the steel biopsy needle—in equation (2). Figure 2h summarizes the sensor voltages measured at similar actuator voltages for artificial tissues with various moduli. Compared with device 1, these systems exhibit comparatively small sensor voltages due to increased stiffness and reduced deformability of the substrate structure (stainless steel has a modulus of ~200 GPa³⁶; PI has a modulus of ~2.5 GPa^{39,37}).

In both cases, the modulus measurements yield properties in near proximity to the actuator/sensor pairs. Placing the probe (device 1) at various levels of injection into an artificial multilayer tissue sample constructed with three different layers of agarose gel (18, 33 and

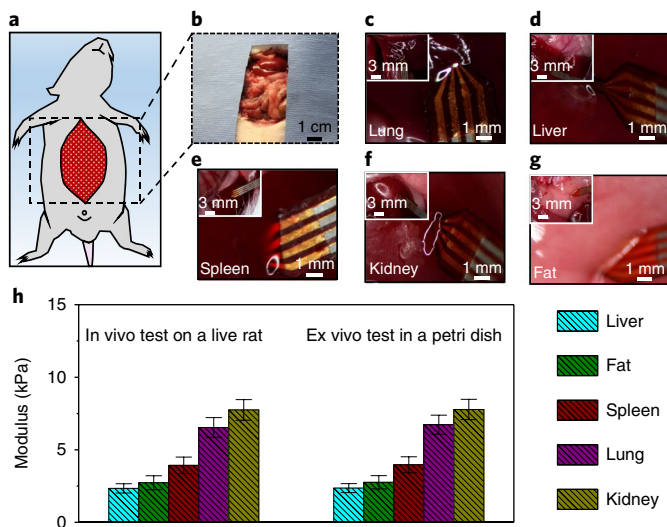


Fig. 3 | In vivo and ex vivo measurements on animal model tissues.

a,b, Schematic diagram (**a**) and an optical image (**b**) of a rodent during measurements with the chest opened. **c–g**, Photographs of a device injected into the lung (**c**), liver (**d**), spleen (**e**), kidney (**f**) and belly fat (**g**). The insets provide unmagnified views. **h**, Results of in vivo modulus measurements on a live rat and ex vivo results of the same organs after explantation. Error bars correspond to calculated standard error deviation for ten measurements.

80 kPa) demonstrates capabilities in depth profiling, as shown in Supplementary Fig. 16. The inset optical images of Supplementary Fig. 16a highlight the injection process. Supplementary Fig. 16b presents the sensor voltage and extracted modulus values as a function of depth. This capability is critically important for investigations of various layered tissue structures that are ubiquitous in biology, and for guidance in biopsies.

In these and other uses, the devices must be well encapsulated to avoid unwanted penetration of bio-fluids into the active regions of the devices³⁸. Mechanical properties of tissues may vary over time due to dehydration, bleeding and/or tissue damage. Tests that involve injection into artificial tissues or fresh explanted biological tissues show continuous, invariant operation for 60 min—significantly longer than the time duration for a typical biopsy (Supplementary Fig. 17). The systems reported here use PI as an encapsulant. Parylene represents an alternative, with improved barrier properties.

Animal model evaluations in vivo and ex vivo. These probes can be inserted percutaneously into a wide range of biological tissues for modulus measurements both in vivo and ex vivo, as shown in rat models in Fig. 3a,b and Supplementary Fig. 18. Figure 3c–g and Supplementary Fig. 19 summarize the results obtained from explanted samples of liver, fat, kidney, spleen and lung, each in a non-diseased state. Modulus values for these organs and tissues are shown in Fig. 3h. The in vivo results, collected on an anaesthetized rat, show that $E_{\text{liver}} = 2.3 \pm 0.2 \text{ kPa}$, $E_{\text{fat}} = 2.4 \pm 0.5 \text{ kPa}$, $E_{\text{spleen}} = 3.9 \pm 0.6 \text{ kPa}$, $E_{\text{lung}} = 6.5 \pm 0.7 \text{ kPa}$ and $E_{\text{kidney}} = 7.8 \pm 0.7 \text{ kPa}$, consistent with ex vivo measurements using the same measurement system and as separately reported based on conventional indentation techniques^{39–41}. Here, the error bars correspond to different measurement sites and are dominated by intrinsic variability associated with the organs themselves.

Measurements on human organ tissues, including cancerous sites. Tests using device 2 on human organ tissues illustrate the potential relevance to clinical practice. The samples include formalin-fixed healthy lung and adrenal gland as summarized in Fig. 4a,b. Comparisons from fresh cirrhotic liver and fresh liver tumour (hepatocellular carcinoma (HCC)) are shown in Fig. 4d,e. Cirrhotic liver exhibits a modulus ~10 kPa, while the modulus of liver tumour is notably higher at ~23 kPa. Tests of pathological tissues clearly show that device 2 can distinguish normal from diseased areas. Figure 4c,f provides images and modulus measurements of a fresh thyroid tissue and a formalin-fixed kidney tissue,

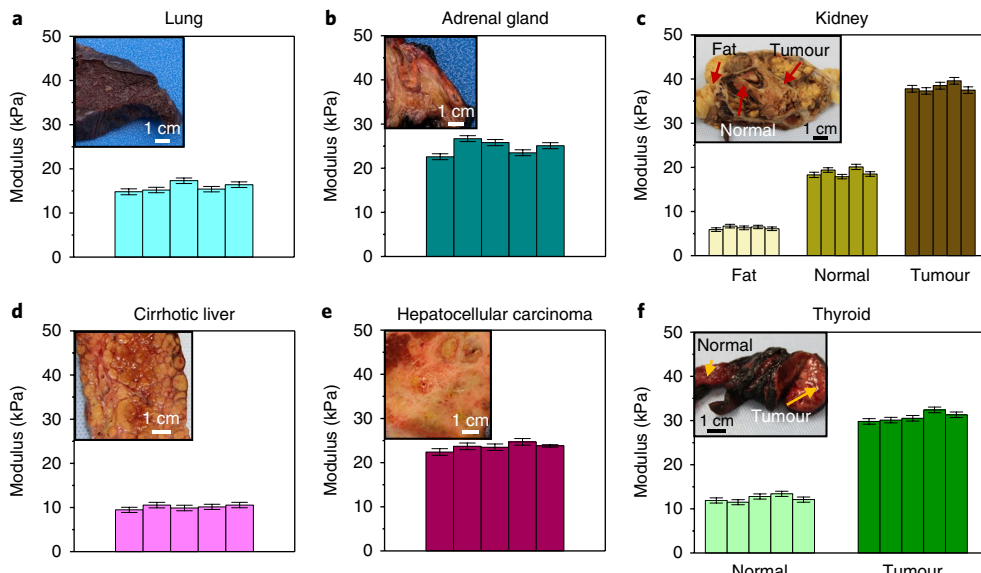


Fig. 4 | Measurements of tissue modulus performed using a sensor system laminated onto a conventional biopsy needle. **a–f**, Modulus values measured on formalin-fixed and fresh tissues. The insets show optical images of the fixed lung tissue (**a**), fixed adrenal gland tissue (**b**), fixed kidney tissue with tumour (**c**), fresh cirrhotic liver (**d**), hepatocellular carcinoma (**e**) and fresh thyroid with tumour (**f**). Error bars correspond to calculated standard error deviation for ten measurements.

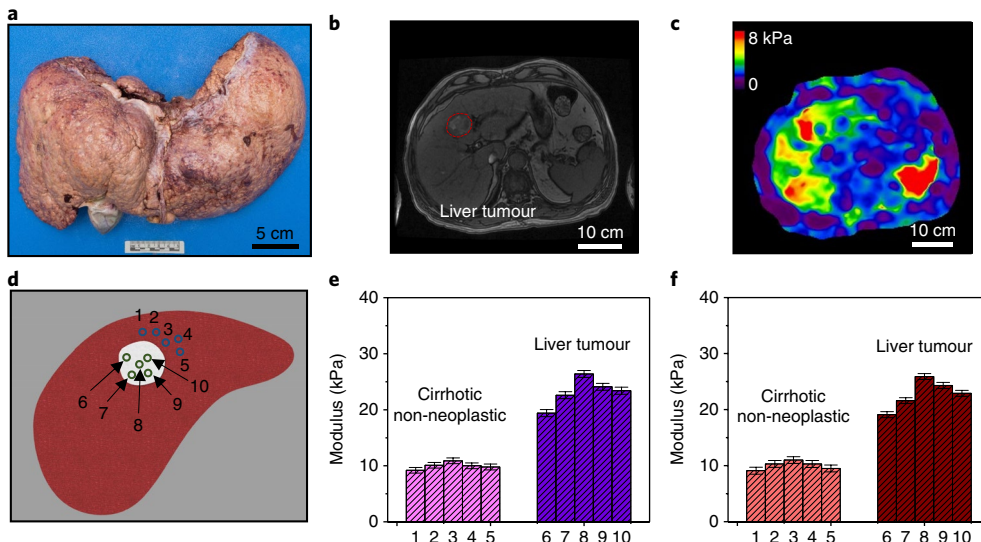


Fig. 5 | Modulus-based biopsy guidance in cancerous human tissue samples. **a**, Photograph of a cirrhotic explanted human liver with a tumour. **b**, Magnetic resonance image of the tumour (red circle) within the liver. **c**, Magnetic resonance elastographs of the cirrhotic liver with tumour, presented as a 2D map of the shear modulus in a plane near the centre of the organ. **d**, Cross-sectional schematic diagram of the sites for measurement using the modulus-sensing probes. **e,f**, Modulus values measured from healthy and cancerous tissues using device 1 (**e**) and device 2 (**f**). Error bars correspond to calculated standard error deviation for ten measurements.

both with tumours. The needle biopsy device is also capable of real-time measurements of modulus as a function of the penetration depth from normal tissue into tumour sites. Supplementary Fig. 20 demonstrates the measurements as the device traverses from cirrhosis liver to a tumour. The results illustrate function on clinically relevant organ tissues, with the ability to distinguish normal from lesion areas, and to provide guidance in biopsies. The liver serves as a model to demonstrate further capabilities in image-guided biopsy tissue targeting, as described next.

Needle biopsy of tumour tissues. The evaluation of a variety of tumour tissues serves as a demonstration in the context of HCC⁴², which was chosen because concern for HCC is a common reason for ordering biopsy procedures⁴³. Specifically, any suspicious liver lesion in patients at risk for HCC requires a biopsy for tissue diagnosis and strict imaging surveillance to prevent its progression⁴⁴. However, conventional biopsies of liver tissue for HCC have high rates of false negatives, and occult lesions <3 cm are particularly difficult to target using ultrasound or computed tomography guidance⁴⁵; HCC is thus a type of cancer for which improved biopsy quality would address an important clinical need.

Although magnetic resonance imaging and MRE can provide high-resolution images of the extent of a tumour, such methods are impractical for guiding a biopsy needle. Therefore, even though computed tomography is inferior to MRE in this context, computed tomography is commonly used because of its wide availability, low cost and fast modes of image acquisition compatible with use during a biopsy. Tests using device 2 demonstrate significant value in this context, as the evaluation of recipient livers with HCC yields modulus values that quantitatively match those extrapolated from MRE (the existing Food and Drug Administration (FDA)-approved procedure for the assessment of cirrhosis⁴⁶). Specifically, MRE measurements of shear modulus (μ)⁴⁷ relate to the Young's modulus in soft tissues via the relationship $E=3\mu$ (ref. ⁴⁶).

Figure 5a shows a photograph of an explanted cirrhotic liver with HCC. This is also shown by magnetic resonance imaging in Fig. 5b. MRE yields a two-dimensional spatial map of the shear modulus across a slice of the liver near its centre, as presented in Fig. 5c and

Supplementary Fig. 21. The application of device 2 yields Young's modulus values for this same tissue sample (Supplementary Fig. 22) in non-tumour cirrhotic areas and tumour areas at different locations to provide at least ten measurements, as shown in Fig. 5d. Device 1 yields additional comparison data. The modulus values for the cirrhotic liver lie in the range 9–11 kPa (Fig. 5e,f), while those of the liver tumour are significantly higher, between 19 and 25 kPa. The modulus values in various areas of the cirrhotic liver fall in a narrow range, with a standard deviation <10%. In contrast, the spatial variability of the liver tumour is as high as ~6 kPa, consistent with the known variations in the stiffness of tumours, where the centre of the tumour is often stiffer than the edge⁴⁸. The results are consistent with the gold standard for mechanical measurements—MRE—via the relationship $E=3\mu$, and they are also comparable to those in the literature^{46,47}. Collectively, these findings clearly indicate that both types of injectable sensor (devices 1 and 2) can be used as a unique tool for tissue pathology studies, such as tumour detection, including needle guidance during biopsy procedures.

Outlook

Cancer is a leading cause of death worldwide, and biopsy procedures are indispensable for diagnosis, assessing treatment response and—in an era of personalized medicine—genetic testing to guide therapy. Accurate tissue biopsy is therefore critical in the management of most cancers. However, centres across the nation and even multi-centre, pan-cancer clinical trials are unable to reduce failed biopsy rates to below 20%⁴⁹. Current imaging modalities for guiding biopsies either do not provide sufficient information or are not suitable for widespread clinical implementation. The results presented here suggest the potential of the miniaturized modulus-sensing device for biopsy guidance on the basis of elastography principles. This work demonstrates the feasibility of detection of HCC in liver tissue, for which false negative results following percutaneous biopsy of small lesions are common. More broadly, microsystem technologies for rapid, high-resolution modulus sensing could find uses across many other scenarios of clinical relevance. Future and ongoing work focuses on the engineering development of multi-function devices that enable the monitoring of temperature and flow rate.

Methods

Preparation of membranes of $\text{Pb}(\text{Zr}_{0.52}\text{Ti}_{0.48})\text{O}_3$ (PZT). The fabrication of PZT membrane actuators and sensors began with the formation of 500-nm-thick films of PZT (MEMS Solution) by sol-gel techniques on oxidized silicon wafers. Sensor and actuator components, each with lateral dimensions of $200\text{ }\mu\text{m} \times 140\text{ }\mu\text{m}$ used parallel-plate type capacitor designs with top and bottom electrodes. First, electron beam deposition formed a bilayer of Au/Cr (200 nm/10 nm) as the top electrode on multilayer stacks of PZT/Pt/Ti/SiO₂ (500 nm/200 nm/5 nm/600 nm). Photolithography (Photoresist (PR) AZ 5214E; Micro Chemicals) and etching (gold: TFA, Transene Company; chrome: OM Group) defined an array of top electrodes (150 $\mu\text{m} \times 100\text{ }\mu\text{m}$, with a square notch of $50\text{ }\mu\text{m} \times 50\text{ }\mu\text{m}$). Additional photopatterning (mask of PR hard baked at 150°C for 5 min) and etching (HNO₃:buffered hydrogen fluoride:deionized water = 1:1:20) defined PZT regions with dimensions of $180\text{ }\mu\text{m} \times 120\text{ }\mu\text{m}$ (with a rectangle of $50\text{ }\mu\text{m} \times 40\text{ }\mu\text{m}$ notch, for the purpose of bottom electrode connection). A final sequence of photopatterning and etching (HCl:HNO₃:deionized water = 3:1:4 at 100°C through a hard-baked mask of AZ4260) defined bottom Pt/Ti electrodes with dimensions of $200\text{ }\mu\text{m} \times 140\text{ }\mu\text{m}$. Next, protecting the PZT with PR (AZ4260) allowed partial undercut removal of the underlying SiO₂ sacrificial layer by immersion in buffered hydrogen fluoride. Removing the PR with acetone enabled patterning of another layer of PR as a top surface encapsulation and perimeter anchor to the underlying wafer. Immersion in dilute hydrofluoric acid (deionized water:49% hydrofluoric acid = 3:1) completely removed the SiO₂, thereby preparing the structures for transfer printing.

Fabrication of the sensor and actuator systems. A layer of photocurable epoxy (SU-8, MicroChem) was photopatterned to serve as a master for moulding surface relief onto a slab of PDMS as a stamp for transfer printing. Specifically, the photopatterning of a 100- μm -thick film of SU-8 100 (MicroChem) spin cast on a polished silicon wafer defined an array of holes with rectangular cross sections ($200\text{ }\mu\text{m} \times 140\text{ }\mu\text{m}$) to yield a corresponding array of posts on the PDMS via drop-casting of a liquid prepolymer mixture (Sylgard 184; Dow Corning, in a 10:1 ratio of prepolymer to curing agent), placement in a vacuum desiccator for 1 h to release bubbles, then curing in an oven at 70°C for 24 h. Peeling the PDMS from the mould and placing it against a glass slide yielded a composite structure with sufficient dimensional stability to allow for accurate alignment. The process for transfer printing followed the scheme depicted in Supplementary Fig. 3, using an automated tool with a digital camera and microscope system for visualization. For device 1, transfer occurred onto a film of PI (75 μm ; DuPont) coated with a thin (1.2 μm) layer of poly(pyromellitic dianhydride-co-4,4'-oxydianiline) amic acid solution baked at 90°C for 30 s to provide a tacky, adhesive surface. The PZT actuator and sensor were transfer printed sequentially. After printing, the entire structure was baked at 150°C on a hot plate for 5 min. The distance between the PZT sensor and actuator was 1 mm. Reactive ion etching (RIE; March) eliminated the layer of PR from the top surfaces of the devices. Spin casting another layer of PI (hard baked at 250°C in a vacuum oven for 75 min) formed a robust encapsulation layer. Openings through the PI, again formed by RIE through a pattern of PR, provided access to the metal electrode contacts. Electron beam evaporation of Au/Cr (200 nm/10 nm) on a patterned layer of PR (AZ2070), followed by immersion in acetone, removed the PR to leave an array of metal interconnects. Another patterned layer of PI (1.2 μm) formed an encapsulation layer over these traces. These overcoats of PI not only prevented direct physical contact of the device structures with biological tissues, but they also provided electrical insulation. The final step involved laser cutting of the PI substrate to form needle geometries with widths of 0.5 mm and lengths of 4 mm. An anisotropic conductive film served as a cable for electrical connection to an external power supply and data acquisition systems. For the ultrathin platforms (3 μm ; PI substrate) of device 2, the devices were first dry etched (RIE; March) through a patterned layer of PR to form a $1.5\text{ mm} \times 4.5\text{ mm}$ area. Retrieval onto a sheet of water-soluble tape (polyvinyl alcohol), followed by electron beam evaporation of Ti/SiO₂ (5 nm/40 nm) on the exposed backside, allowed adhesive transfer onto a 50- μm -thick film of PDMS cast on a layer of PI on a glass slide to prevent any wrinkling or folding. Reactions between hydroxyl groups on the PDMS and SiO₂ surfaces led to strong bonding after baking in an oven at 70°C for 10 min. Immersion in hot water removed the polyvinyl alcohol. Mounting devices and PDMS on the biopsy needle used a similar procedure. Finally, the edge of the device was sealed by PDMS to ensure good adhesion between the device and biopsy needle.

Poling the PZT. Poling involved the application of a static electric field (200 kVcm^{-1}) at 150°C for 2 h to PZT films between the bottom and top contacts of Ti/Pt (5 nm/200 nm) and Cr/Au (10 nm/200 nm), respectively.

Device operation and data collection. The devices were implanted into either artificial or organ tissues. A waveform generator (Keithley 3390), a digital lock-in amplifier (SR830; Stanford Research Systems), digital multimeters (ADIInstruments) and a laptop computer with a custom programme (LabVIEW, National Instruments) enabled the collection of data from the sensors and supply of voltage to the actuators.

Preparation of artificial tissue samples. Agarose gel (Sigma) and PDMS provided two different types of artificial tissue sample. Agarose gel tissue samples were prepared by dissolving powdered agarose in deionized water at 100°C while vigorously stirring for 3 h until the solution became transparent. Solutions with different concentrations formed in this way were slowly cooled to room temperature, poured into moulds or small vials and then stored in a refrigerator overnight. For the case of PDMS, sample preparation began with the mixing of various ratios of prepolymer to curing agent, storing in a vacuum desiccator for 30 min, then pouring into the moulds and curing in an oven at 70°C for 24 h.

DMA. DMA (Q800 DMA; TA Instruments) yielded Young's moduli via analysis of quasi-static stress-strain curves. The measurements used the DMA film tension clamp in ambient conditions at a strain rate of 1 \% min^{-1} to a maximum value of 10%.

Animal model in vivo and ex vivo tests. The experiments were conducted in accordance with the ethical guidelines of the National Institutes of Health and with the approval of the Animal Care and Use Committee of Mayo Clinic's institutional review board. For in vivo and ex vivo device validation, an anaesthetized Sprague Dawley rat was placed in a supine position over a warming platform. A mid-abdominal incision was made and the abdominal wall was retracted. Blunt dissection was used to expose the abdominal fat, liver, spleen and kidneys. The modulus sensor was inserted directly into each organ using a blunt forceps. Once the abdominal organ modulus measurements were acquired, a thoracic incision was made to insert the sensor into the lung tissue. Following in vivo measurements, the rat was euthanized and each organ was removed and transferred to petri dishes to obtain ex vivo measurements. The organ removal required less than 3 min and the ex vivo test occurred immediately after removal. The total ex vivo measuring time was 10 min.

Human organ tissue tests. Following Mayo Clinic's institutional review board approval, we used samples of residual discarded tissue, including fresh and formalin-fixed tissue—specifically, the liver, lung, kidney, thyroid gland and adrenal gland. Tumour tissue was present in the liver, thyroid and kidney specimens. The institutional review board did not require informed consent from tissue donors because de-identified residual discarded clinical tissue was used in the experiments. The use of magnetic resonance imaging and MRE images of the livers was also approved.

Life Sciences Reporting Summary. Further information on experimental design is available in the Life Sciences Reporting Summary.

Data availability. The authors declare that all data supporting the findings of this study are available within the paper and its Supplementary Information.

Received: 7 September 2017; Accepted: 22 January 2018;
Published online: 26 February 2018

References

- Maharaj, B. et al. Sampling variability and its influence on the diagnostic yield of percutaneous needle biopsy of the liver. *Lancet* **327**, 523–525 (1986).
- Saggese, M., Dua, D., Simmons, E., Lemech, C. & Arkenau, H.-T. Research biopsies in the context of early phase oncology studies: clinical and ethical considerations. *Oncol. Rev.* **7**, e5 (2013).
- Regev, A. et al. Sampling error and intraobserver variation in liver biopsy in patients with chronic HCV infection. *Am. J. Gastroenterol.* **97**, 2614–2618 (2002).
- Shyamala, K., Girish, H. C. & Murgod, S. Risk of tumor cell seeding through biopsy and aspiration cytology. *J. Int. Soc. Prev. Community Dent.* **4**, 5–11 (2014).
- National Cancer Institute NCI-MATCH Trial (Molecular Analysis for Therapy Choice) (2017); <https://www.cancer.gov/about-cancer/treatment/clinical-trials/nci-supported/nci-match>
- Rago, T., Santini, F., Scutari, M., Pinchera, A. & Vitti, P. Elastography: new developments in ultrasound for predicting malignancy in thyroid nodules. *J. Clin. Endocrinol. Metab.* **92**, 2917–2922 (2007).
- Gerughty, P. R. et al. CT-guided transthoracic needle aspiration biopsy of pulmonary nodules: needle size and pneumothorax rate. *Radiology* **229**, 475–481 (2003).
- Picarelli, A. et al. Production of antiendomysial antibodies after in-vitro gliadin challenge of small intestine biopsy samples from patients with coeliac disease. *Lancet* **348**, 1065–1067 (1996).
- Discher, D. E., Janmey, P. & Wang, Y. L. Tissue cells feel and respond to the stiffness of their substrate. *Science* **310**, 1139–1143 (2005).
- Abramowitch, S. D., Feola, A., Jallah, Z. & Moalli, P. A. Tissue mechanics, animal models, and pelvic organ prolapse: a review. *Eur. J. Obstet. Gynecol. Reprod. Biol.* **144**, S146–S158 (2009).

11. Fung, Y. C. *Biomechanics: Mechanical Properties of Living Tissues* (Springer, New York, 2013).
12. Ziol, M. et al. Noninvasive assessment of liver fibrosis by measurement of stiffness in patients with chronic hepatitis C. *Hepatology* **41**, 48–54 (2005).
13. O'Rourke, M. F. & Safar, M. E. Relationship between aortic stiffening and microvascular disease in brain and kidney: cause and logic of therapy. *Hypertension* **46**, 200–204 (2005).
14. Li, M. et al. Modeling lung deformation: a combined deformable image registration method with spatially varying Young's modulus estimates. *Med. Phys.* **40**, 081902 (2013).
15. Miller, K. & Chinzei, K. Mechanical properties of brain tissue in tension. *J. Biomech.* **35**, 483–490 (2002).
16. Wickramaratne, D. et al. Fine needle elastography (FNE) device for biomechanically determining local variations of tissue mechanical properties. *J. Biomech.* **48**, 81–88 (2015).
17. Yeh, W.-C. et al. Elastic modulus measurements of human liver and correlation with pathology. *Ultrasound Med. Biol.* **28**, 467–474 (2002).
18. Diridollou, S. et al. In vivo model of the mechanical properties of the human skin under suction. *Skin Res. Technol.* **6**, 214–221 (2000).
19. Samani, A., Zubovits, J. & Plewes, D. Elastic moduli of normal and pathological human breast tissues: an inversion-technique-based investigation of 169 samples. *Phys. Med. Biol.* **52**, 1565–1576 (2007).
20. Rho, J. Y., Roy, M. E., Tsui, T. Y. & Pharr, G. M. Elastic properties of microstructural components of human bone tissue as measured by nanoindentation. *J. Biomed. Mater. Res. A* **45**, 48–54 (1999).
21. Nightingale, K., Soo, M. S., Nightingale, R. & Trahey, G. Acoustic radiation force impulse imaging: in vivo demonstration of clinical feasibility. *Ultrasound Med. Biol.* **28**, 227–235 (2002).
22. Castera, L., Vilgrain, V. & Angulo, P. Noninvasive evaluation of NAFLD. *Nat. Rev. Gastroenterol. Hepatol.* **10**, 666–675 (2013).
23. Leung, V. Y. et al. Quantitative elastography of liver fibrosis and spleen stiffness in chronic hepatitis B carriers: comparison of shear-wave elastography and transient elastography with liver biopsy correlation. *Radiology* **269**, 910–918 (2013).
24. Muthupillai, R. et al. Magnetic resonance elastography by direct visualization of propagating acoustic strain waves. *Science* **269**, 1854–1857 (1995).
25. Sinkus, R. et al. High-resolution tensor MR elastography for breast tumour detection. *Phys. Med. Biol.* **45**, 1649 (2000).
26. Goss, B. C., McGee, K. P., Ehman, E. C., Manduca, A. & Ehman, R. L. Magnetic resonance elastography of the lung: technical feasibility. *Magn. Reson. Med.* **56**, 1060–1066 (2006).
27. Agid, R. et al. CT-guided biopsy with cutting-edge needle for the diagnosis of malignant lymphoma: experience of 267 biopsies. *Clin. Radiol.* **58**, 143–147 (2003).
28. Mirnezami, R., Nicholson, J. & Darzi, A. Preparing for precision medicine. *N. Engl. J. Med.* **366**, 489–491 (2012).
29. Dagdeviren, C. et al. Conformal piezoelectric systems for clinical and experimental characterization of soft tissue biomechanics. *Nat. Mater.* **14**, 728–736 (2015).
30. Carlson, A., Bowen, A. M., Huang, Y., Nuzzo, R. G. & Rogers, J. A. Transfer printing techniques for materials assembly and micro/nanodevice fabrication. *Adv. Mater.* **24**, 5284–5318 (2012).
31. Jeong, J.-W. et al. Wireless optofluidic systems for programmable in vivo pharmacology and optogenetics. *Cell* **162**, 662–674 (2015).
32. Koh, A. et al. Ultrathin injectable sensors of temperature, thermal conductivity, and heat capacity for cardiac ablation monitoring. *Adv. Healthc. Mater.* **5**, 373–381 (2016).
33. Wang, Z., Volinsky, A. A. & Gallant, N. D. Nanoindentation study of polydimethylsiloxane elastic modulus using Berkovich and flat punch tips. *J. Appl. Polym. Sci.* **132**, 41384 (2015).
34. Mauck, R. L. et al. Functional tissue engineering of articular cartilage through dynamic loading of chondrocyte-seeded agarose gels. *J. Biomech. Eng.* **122**, 252–260 (2000).
35. Normand, V., Lootens, D. L., Amici, E., Plucknett, K. P. & Aymard, P. New insight into agarose gel mechanical properties. *Biomacromolecules* **1**, 730–738 (2000).
36. Travessa, D., Ferrante, M. & den Ouden, G. Diffusion bonding of aluminium oxide to stainless steel using stress relief interlayers. *Mater. Sci. Eng. A* **337**, 287–296 (2002).
37. Purton, D. & Payne, J. Comparison of carbon fiber and stainless steel root canal posts. *Quintessence Int.* **27**, 93–97 (1996).
38. Fang, H. et al. Capacitively coupled arrays of multiplexed flexible silicon transistors for long-term cardiac electrophysiology. *Nat. Biomed. Eng.* **1**, 0038 (2017).
39. Rotsch, C., Braet, F., Wisse, E. & Radmacher, M. AFM imaging and elasticity measurements on living rat liver macrophages. *Cell Biol. Int.* **21**, 685–696 (1997).
40. Adler, A., Cowley, E. A., Bates, J. H. T. & Eidelman, D. H. Airway-parenchymal interdependence after airway contraction in rat lung explants. *J. Appl. Physiol.* **85**, 231–237 (1998).
41. Wyss, H. M. et al. Biophysical properties of normal and diseased renal glomeruli. *Am. J. Physiol. Cell Physiol.* **300**, C397–C405 (2011).
42. Bruix, J. & Sherman, M. Management of hepatocellular carcinoma: an update. *Hepatology* **53**, 1020–1022 (2011).
43. Liaw, Y.-F. & Chu, C.-M. Hepatitis B virus infection. *Lancet* **373**, 582–592 (2009).
44. Bravo, A. A., Sheth, S. G. & Chopra, S. Liver biopsy. *N. Engl. J. Med.* **344**, 495–500 (2001).
45. Ahrrar, K. in *Percutaneous Image-Guided Biopsy* 19–32 (Springer, New York, 2014).
46. Mariappan, Y. K., Glaser, K. J. & Ehman, R. L. Magnetic resonance elastography: a review. *Clin. Anat.* **23**, 497–511 (2010).
47. Manduca, A. et al. Magnetic resonance elastography: non-invasive mapping of tissue elasticity. *Med. Image Anal.* **5**, 237–254 (2001).
48. Stylianopoulos, T. et al. Causes, consequences, and remedies for growth-induced solid stress in murine and human tumors. *Proc. Natl Acad. Sci. USA* **109**, 15101–15108 (2012).
49. Do, K., O'Sullivan Coyne, G. & Chen, A. P. An overview of the NCI precision medicine trials—NCI MATCH and MPACT. *Clin. Clin. Oncol.* **4**, 31 (2015).

Acknowledgements

This work was supported by the Center for Bio-Integrated Electronics. R.O. acknowledges National Institutes of Health grants R01HL137193, R01EB24403, R21EB021148 and R03CA172738, and Mayo Clinic. R.S. acknowledges support from the Engineering and Physical Sciences Research Council (grant number EP/L016028/1) and China Scholarship Council. L.T. acknowledges support from a Beckman Institute postdoctoral fellowship at the University of Illinois Urbana-Champaign. Y.H. acknowledges support from the National Science Foundation (grant numbers 1400169, 1534120 and 1635443) and National Institutes of Health (grant number R01EB019337). The authors acknowledge N. Pallace (Media Support Services at Mayo Clinic) for expert photography during the experiments.

Author contributions

X.Y., H.W., X.N., Y.H., R.O. and J.A.R. designed the experiment and wrote the manuscript. X.Y., H.W., X.N., R.S., M.S., H.A., Y.Y., A.K., C.M.L., A.C.S., P.T. and R.O. performed the experiments and analysed the experimental data. H.W. led the structural designs and mechanics modelling, with assistance from J.Y. L.T. and M.P. contributed to the analysis of the experimental results.

Competing interests

The authors declare no competing interests.

Additional information

Supplementary information is available for this paper at <https://doi.org/10.1038/s41551-018-0201-6>.

Reprints and permissions information is available at www.nature.com/reprints.

Correspondence and requests for materials should be addressed to Y.H. or R.O. or J.A.R.

Publisher's note: Springer Nature remains neutral with regard to jurisdictional claims in published maps and institutional affiliations.

In the format provided by the authors and unedited.

Needle-shaped ultrathin piezoelectric microsystem for guided tissue targeting via mechanical sensing

Xinge Yu^{1,2,19}, Heling Wang^{3,4,5,19}, Xin Ning^{2,19}, Rujie Sun^{2,6}, Hassan Albadawi⁷, Marcela Salomao⁸, Alvin C. Silva⁹, Yang Yu^{2,10}, Limei Tian^{2,11}, Ahyeon Koh¹², Chan Mi Lee², Aditya Chempakasseril², Peilin Tian², Matt Pharr¹³, Jianghong Yuan^{3,4,5,14}, Yonggang Huang^{3,4,5*}, Rahmi Oklu¹⁰  ^{7*} and John A. Rogers^{1,2,5,15,16,17,18*}

¹Simpson Querrey Center and Feinberg School of Medicine, Center for Bio-Integrated Electronics, Northwestern University, Evanston, IL, USA. ²Department of Materials Science and Engineering, Frederick Seitz Materials Research Laboratory, University of Illinois at Urbana-Champaign, Urbana, IL, USA.

³Department of Civil and Environmental Engineering, Northwestern University, Evanston, IL, USA. ⁴Department of Mechanical Engineering, Northwestern University, Evanston, IL, USA. ⁵Department of Materials Science and Engineering, Northwestern University, Evanston, IL, USA. ⁶Advanced Composites Centre for Innovation and Science, University of Bristol, Bristol, UK. ⁷Division of Vascular and Interventional Radiology, Minimally Invasive Therapeutics Laboratory, Mayo Clinic, Phoenix, AZ, USA. ⁸Department of Pathology, Mayo Clinic, Phoenix, AZ, USA. ⁹Division of Abdominal Imaging, Mayo Clinic, Phoenix, AZ, USA. ¹⁰Department of Materials Science and Engineering, Tsinghua University, Beijing, China. ¹¹Beckman Institute for Advanced Science and Technology, University of Illinois at Urbana-Champaign, Urbana, IL, USA. ¹²Department of Biomedical Engineering, Binghamton University, Binghamton, NY, USA. ¹³Department of Mechanical Engineering, Texas A&M University, College Station, TX, USA. ¹⁴Center for Mechanics and Materials, and Applied Mechanics Laboratory, Department of Engineering Mechanics, Tsinghua University, Beijing, China. ¹⁵Department of Biomedical Engineering, Northwestern University, Evanston, IL, USA. ¹⁶Department of Neurological Surgery, Northwestern University, Evanston, IL, USA. ¹⁷Department of Chemistry, Northwestern University, Evanston, IL, USA. ¹⁸Department of Electrical Engineering and Computer Science, Northwestern University, Evanston, IL, USA. ¹⁹These authors contributed equally: Xinge Yu, Heling Wang and Xin Ning. *e-mail: y-huang@northwestern.edu; oklu.rahmi@mayo.edu; jrogers@northwestern.edu

List of contents:

Supplementary Note 1. Finite element analysis (FEA) method and condition.

Supplementary Note 2. FEA validation of the scaling law.

Figure S1. Schematic illustration of procedures for fabricating PZT membrane inks on a SiO₂/Si wafer. a. Schematic diagram of cross section view for a PZT wafer with structure Au/Cr/PZT/Pt/Ti/SiO₂/Si. b. The capacitor structure PZT membranes were patterned and defined by photolithography technique. c. Partial under cut etching of SiO₂ sacrificial layer by buffered oxide etchant. d. Final PZT membrane inks formed by fully under cut etching of SiO₂ sacrificial layer with dilute HF solution.

Figure S2. Optical images of PZT membrane inks. a. PZT membrane inks array. b. Zoom in view of a PZT membrane.

Figure S3. Representation of transfer printing PZT membranes using a stamp with a post, showing individual process steps. a. Translation and Alignment to PZT membranes donor wafer. b. Selective engagement with one PZT membrane. c. a PZT membrane retrieval from donor wafer and contact to transfer onto polyimide (PI) acceptor substrate. d. e. Repeat cycles of steps a to c, zoom in view shows the two PZTs which will act as the sensor and actuator.

Figure S4. Schematic illustration of sensors/actuators encapsulation and electrodes formation process. a. a PZT membrane on polyimide (PI) substrate. b. First encapsulation PI layer spun and cured on top of the PZT membrane, then patterned using photo resist (PR). c. Opening to holes for cathode and anode connection by dry etching. d. Patterning PI for metallic interconnection wire deposition. e. Cr(10 nm)/Au(200 nm) interconnection wire deposition by E-beam onto the PR and then remove additional PR by lift off technique. f. Final PI encapsulation layer deposited onto the devices to prevent influence of liquid during test.

Figure S5. Modulus probe design and images. a. Design of 6 modulus probes array for laser cut. b. Photograph of modulus probe devices done by laser cut. c. SEM image of a modulus probe device. d, e. Zoom in view of the modulus probe device, shown sensor area (c), and actuator area (d).

Figure S6. Photography of modulus sensor devices. a. Free standing polyimide (PI) supporting layer based device. b. Biopsy needle based device.

Figure S7. a. The nonlinear single-variable function G in the scaling law, determined by FEA. b. Simulation result of $V_{\text{sensor}}/V_{\text{actuator}}$ as a function of modulus.

Figure S8. Validation of the scaling law. a. validate that the function G depends only on a single combination of parameters, $(E_{\text{Tissue}}d^3)/(E_{\text{PI}}h_{\text{PI}}^3)$. b. Validate the linear proportionality between the sensor voltage and $(A_{\text{PZT}}h_{\text{PZT}})/(E_{\text{PI}}h_{\text{PI}}d^2)$.

Figure S9. Prediction of the critical tissue modulus by the scaling law (black solid lines) and the FEA based on the geometrical dimensions of the device in the main text (red dots). a. Influence of the needle substrate modulus. b. Influence of the needle substrate thickness. c. Influence of spacing between the actuator and the sensor.

Figure S10. FEA prediction of the output voltage as a function of the tissue modulus for a small sample (size 1.0 mm × 1.0 mm × 1.5 mm)

Figure S11. Tension stress-strain plots of artificial agarose gel in quasi-static strain rate regimes, with different modulus values.

Figure S12. Experimental and theoretical analysis of the free standing device operation. Voltage output of sensor as a function of actuator voltage, measured on ten different agarose gels with known moduli, separately evaluated by quasi-static dynamical mechanical analysis shown in Figure S11. Here, the symbols and lines correspond to experimental (E) and theoretical (T) results, respectively. Error bars correspond to calculated standard error deviation.

Figure S13. The mechanism of deformation for the modulus sensors integrated on a biopsy needle. The red arrows indicate that the deformation induced by the actuator is transferred to the sensor mainly via the deformation of the tissue and also the PDMS below the PI substrate.

Figure S14. Theoretical analysis of biopsy needle based modulus sensor devices. a. Influence of the PDMS modulus on the sensor voltage. b. Influence of the PDMS thickness on the sensor voltage.

Figure S15. Theoretical analysis of V_{sensor} as a function of modulus, with actuator voltage of 5V.

Figure S16. Experimental analysis and modulus measurements of multilayer artificial tissues. a. Modulus measurement on a multilayer sample, with three different modulus of 18, 33, and 80 kPa. b. Sensor voltage and modulus values at an actuation voltage of 5V, as a function of inject depth of the multilayer sample.

Figure S17. Modulus measurements modulus as function of time for 60 minutes. a. Measured on artificial agarose gel tissues with different modulus values. b. Measured on big tissues, including liver, fat, kidney, and muscle.

Figure S18. Illustration of surgical procedures for modulus measurement on the rat.

Figure S19. Ex-vivo measurement of organ tissues of the rat. Device insert and measure on liver, a, lung b, spleen c, fat d, and kidney e.

Figure S20. Real-time modulus measurement by a biopsy needle device. The device traverse from cirrhosis liver to tumor. Error bars correspond to calculated standard error deviation.

Figure S21. Images of a cirrhotic liver with hepatocellular carcinoma. a. Measured by Magnetic resonance image (MRI). b. Measured by Magnetic resonance electrography (MRE), shown stiffness mapping of the whole cross section of the patient.

Figure S22. Image-guided modulus test. a,b, Photographs of a free standing device (device 1) injected into the non-tumor area of liver (a), and tumor (b). c,d, Photographs of a biopsy needle device (device 2) injected into the non-tumor area of liver (c), and tumor (d).

Supplementary Note 1: Finite element analysis (FEA) method and condition

FEA was conducted using the commercial software ABAQUS (version 6.14, Standard). The end of the needle outside the tissue was fixed to constrain the rigid body motion. Since the deformation was very small (strain <0.1 %), linear coupled mechanical-electric analysis was used to obtain the deformation and sensor voltage. The actuator and sensor were modelled by the linear piezoelectric material, and the tissue, PI and metals were modelled by the linear elastic material. The number of mesh in the model was $\sim 10^6$, with refinement around the region with the actuator and the sensor such that the minimum mesh size was 1/10 of the actuator/sensor size. The mesh convergence of the simulation was guaranteed for all cases.

3D solid elements are used to model the tissue and 3D shell elements are used to model the needle substrate, the actuator, the sensor and the electrode (Ti, Pt, Cr and Cu), with Figure S5 showing the layout. The needle is perfectly bonded to the tissue without relative slipping in FEA.

The material parameters are $E_{\text{PI}}=2.5 \text{ GPa}$, $\nu_{\text{PI}}=0.34$, $E_{\text{Ti}}=110 \text{ GPa}$, $\nu_{\text{Ti}}=0.32$, $E_{\text{Pt}}=168 \text{ GPa}$, $\nu_{\text{Pt}}=0.38$, $E_{\text{Cr}}=279 \text{ GPa}$, $\nu_{\text{Cr}}=0.21$, $E_{\text{Cr}}=117 \text{ GPa}$, $\nu_{\text{Cu}}=0.36$. The constitutive model for PZT is

$$\begin{Bmatrix} \sigma_{11} \\ \sigma_{22} \\ \sigma_{33} \\ \sigma_{23} \\ \sigma_{31} \\ \sigma_{12} \end{Bmatrix} = \begin{Bmatrix} C_{11} & C_{12} & C_{13} & 0 & 0 & 0 \\ C_{12} & C_{11} & C_{13} & 0 & 0 & 0 \\ C_{13} & C_{13} & C_{33} & 0 & 0 & 0 \\ 0 & 0 & 0 & C_{44} & 0 & 0 \\ 0 & 0 & 0 & 0 & C_{44} & 0 \\ 0 & 0 & 0 & 0 & 0 & C_{66} \end{Bmatrix} \begin{Bmatrix} \varepsilon_{11} \\ \varepsilon_{22} \\ \varepsilon_{33} \\ 2\varepsilon_{23} \\ 2\varepsilon_{31} \\ 2\varepsilon_{12} \end{Bmatrix} - \begin{Bmatrix} 0 & 0 & e_{31} \\ 0 & 0 & e_{31} \\ 0 & 0 & e_{33} \\ 0 & e_{15} & 0 \\ e_{15} & 0 & 0 \\ 0 & 0 & 0 \end{Bmatrix} \begin{Bmatrix} E_1 \\ E_2 \\ E_3 \end{Bmatrix} \quad (\text{S1})$$

$$\begin{Bmatrix} D_1 \\ D_2 \\ D_3 \end{Bmatrix} = \begin{Bmatrix} 0 & 0 & 0 & 0 & e_{15} & 0 \\ 0 & 0 & 0 & e_{15} & 0 & 0 \\ e_{31} & e_{31} & e_{33} & 0 & 0 & 0 \end{Bmatrix} \begin{Bmatrix} \varepsilon_{11} \\ \varepsilon_{22} \\ \varepsilon_{33} \\ 2\varepsilon_{23} \\ 2\varepsilon_{31} \\ 2\varepsilon_{12} \end{Bmatrix} + \begin{Bmatrix} k_{11} & 0 & 0 \\ 0 & k_{11} & 0 \\ 0 & 0 & k_{33} \end{Bmatrix} \begin{Bmatrix} E_1 \\ E_2 \\ E_3 \end{Bmatrix} \quad (\text{S2})$$

where σ_{ij} , ε_{ij} , E_i and D_i are the stress, strain, electrical field and electrical displacement respectively. The elastic parameters are $C_{11}=110$ GPa, $C_{12}=63$ GPa, $C_{13}=64$ GPa, $C_{33}=100$ GPa, $C_{44}=20$ GPa and $C_{66}=(C_{11}-C_{12})/2$. The piezoelectric parameters are $e_{31}=-9.6$ N/(V·m), $e_{33}=15.1$ N/(V·m), and $e_{15}=12.0$ N/(V·m). The dielectric parameters are $k_{33}=852\varepsilon_0$, where ε_0 is the vacuum permittivity.

Supplementary Note 2: FEA validation of the scaling law

The scaling law Eq. (1) in the main text is validated by FEA for $h_{\text{PZT}} \ll h_{\text{PI}} \ll w_{\text{PI}}, L_{\text{PI}}$, and $h_{\text{PZT}} \ll L_{\text{PZT}}, w_{\text{PZT}} \ll d \ll w_{\text{PI}}, L_{\text{PI}}$. First, the function G is validated to depend only on a single combination of parameters, $(E_{\text{Tissue}}d^3)/(E_{\text{PI}}h_{\text{PI}}^3)$. Among four parameters E_{Tissue} , d , E_{PI} and h_{PI} , one changes while the other three are fixed. The sensor voltage obtained by FEA then gives G , which is shown by the $G \sim (E_{\text{Tissue}}d^3)/(E_{\text{PI}}h_{\text{PI}}^3)$ plot in Figure S2a. It is clear that all data points fall on the same curve, confirming that G depends only on $G \sim (E_{\text{Tissue}}d^3)/(E_{\text{PI}}h_{\text{PI}}^3)$.

The linear proportionality between the sensor voltage and $(A_{\text{PZT}}h_{\text{PZT}})/(E_{\text{PI}}h_{\text{PI}}d^2)$ is verified next. With G fixed, among five parameters d , E_{PI} , h_{PI} , A_{PZT} and h_{PZT} , one changes while the other four are fixed. All data points obtained by FEA fall on the straight line in Figure S2b, confirming that the sensor voltage is linearly proportional to $(A_{\text{PZT}}h_{\text{PZT}})/(E_{\text{PI}}h_{\text{PI}}d^2)$.

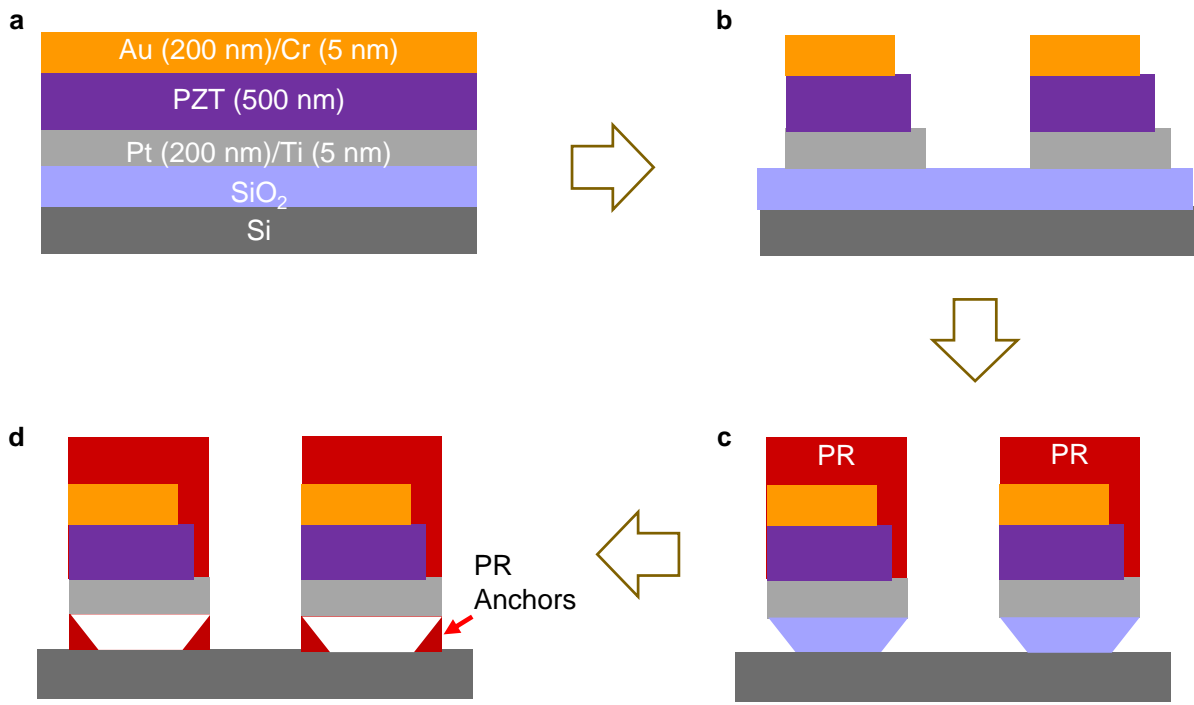


Figure S1. Schematic illustration of procedures for fabricating PZT membrane inks on a SiO₂/Si wafer. **a.** Schematic diagram of cross section view for a PZT wafer with structure Au/Cr/PZT/Pt/Ti/SiO₂/Si. **b.** The capacitor structure PZT membranes were patterned and defined by photolithography technique. **c.** Partial under cut etching of SiO₂ sacrificial layer by buffered oxide etchant. **d.** Final PZT membrane inks formed by fully under cut etching of SiO₂ sacrificial layer with dilute HF solution.

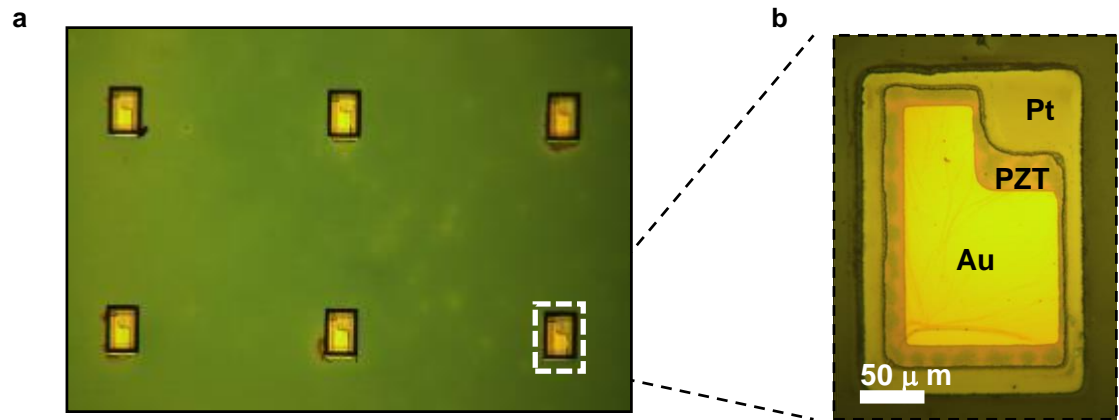


Figure S2. Optical images of PZT membrane inks. **a.** PZT membrane inks array. **b.** Zoom in view of a PZT membrane

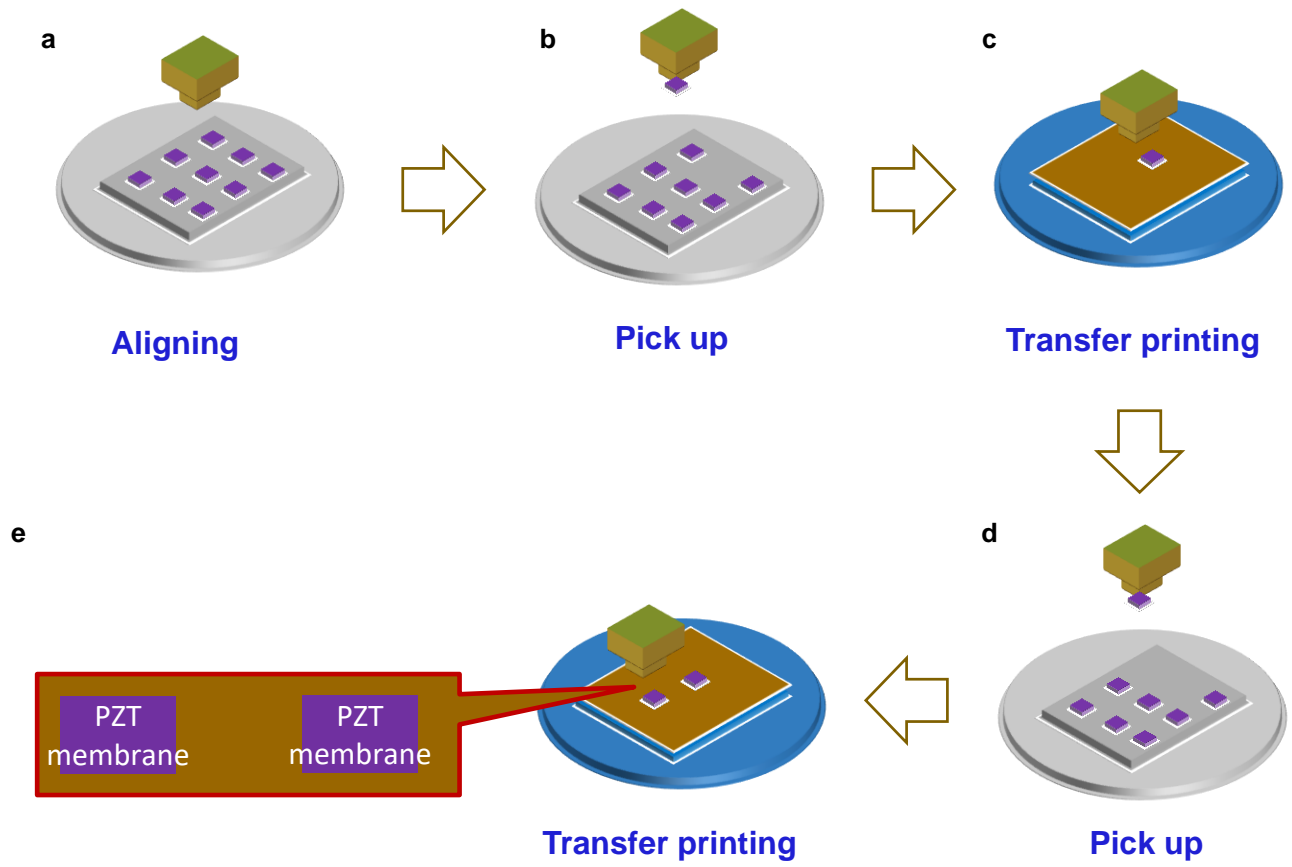


Figure S3. Representation of transfer printing PZT membranes using a stamp with a post, showing individual process steps. **a.** Translation and Alignment to PZT membranes donor wafer. **b.** Selective engagement with one PZT membrane. **c.** a PZT membrane retrieval from donor wafer and contact to transfer onto polyimide (PI) acceptor substrate. **d.** **e.** Repeat cycles of steps a to c, zoom in view shows the two PZTs which will act as the sensor and actuator.

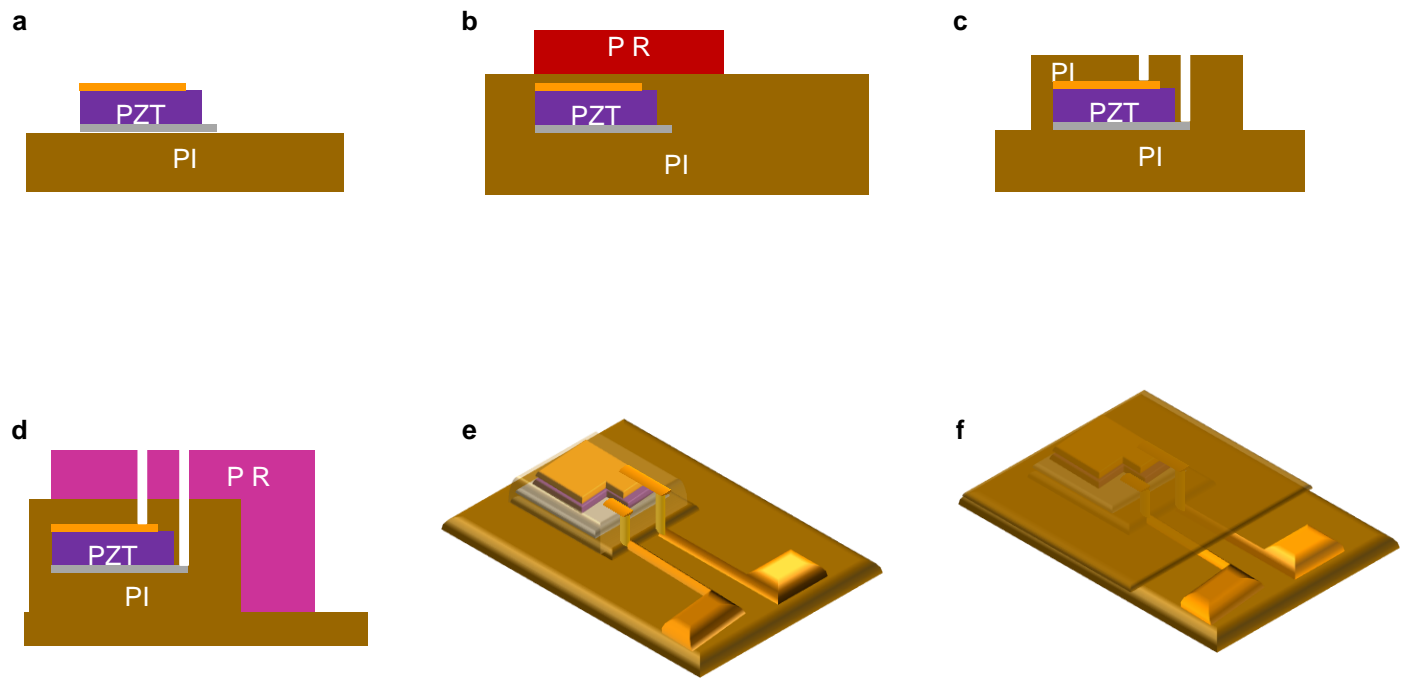


Figure S4. Schematic illustration of sensors/actuators encapsulation and electrodes formation process. **a.** a PZT membrane on polyimide (PI) substrate. **b.** First encapsulation PI layer spun and cured on top of the PZT membrane, then patterned using photo resist (PR). **c.** Opening to holes for cathode and anode connection by dry etching. **d.** Patterning PI for metallic interconnection wire deposition. **e.** Cr(10 nm)/Au(200 nm) interconnection wire deposition by E-beam onto the PR and then remove additional PR by lift off technique. **f.** Final PI encapsulation layer deposited onto the devices to prevent influence of liquid during test.

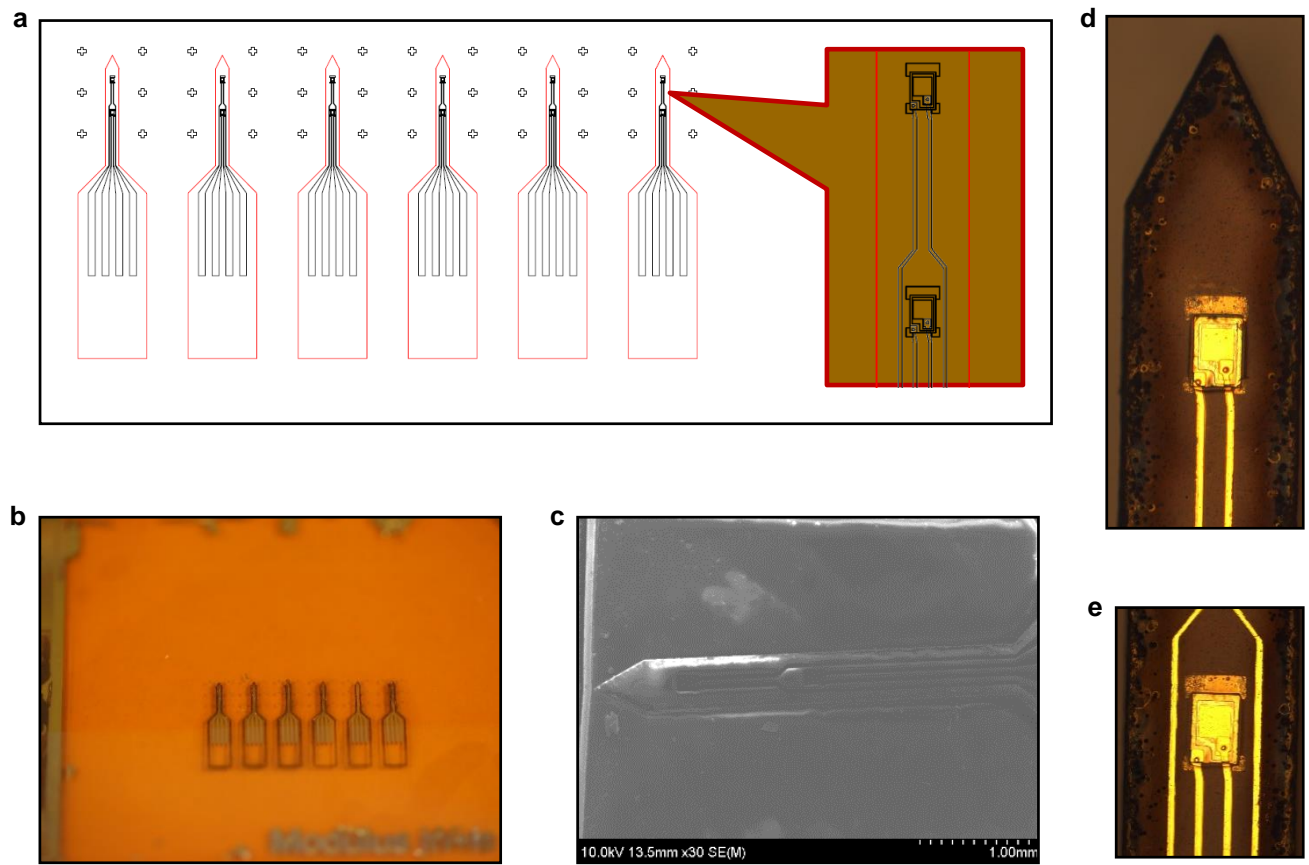


Figure S5. Modulus probe. **a.** Design of 6 modulus probes array for laser cut. **b.** Photograph of modulus probe devices done by laser cut. **c.** SEM image of a modulus probe device. **d, e.** Zoom in view of the modulus probe device, shown sensor area (c), and actuator area (d).

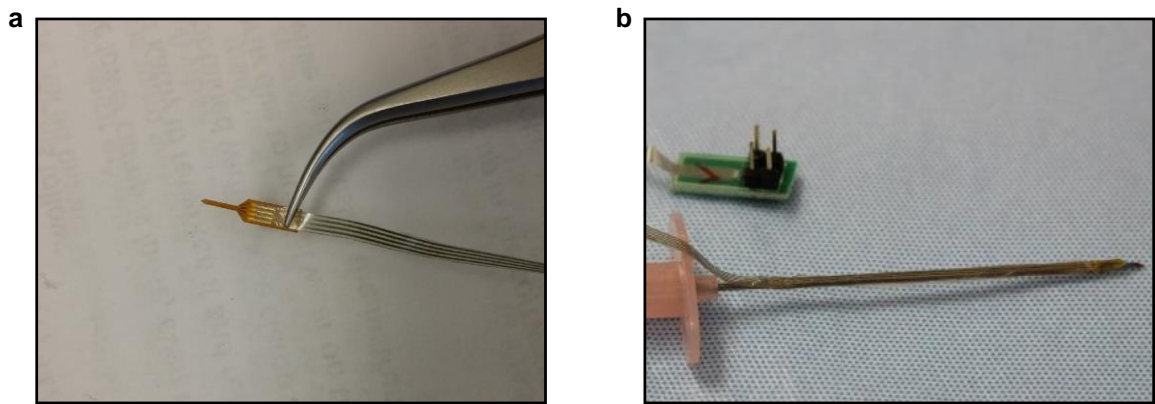


Figure S6. Photography of modulus sensor devices. **a.** Free standing polyimide (PI) supporting layer based device. **b.** Biopsy needle based device.

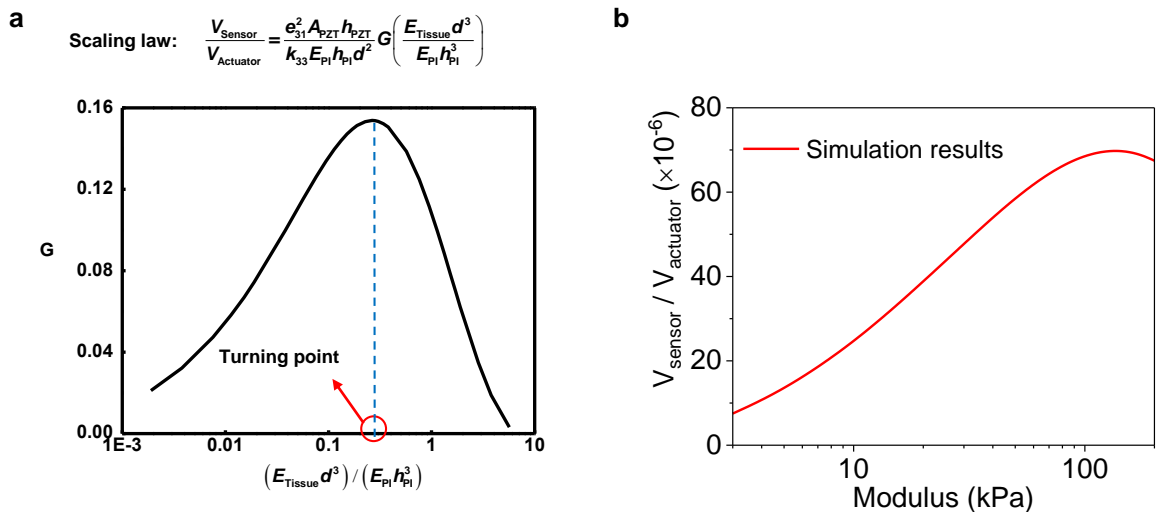


Figure S7. **a.** The nonlinear single-variable function G in the scaling law, determined by FEA. **b.** Simulation result of $V_{\text{sensor}}/V_{\text{actuator}}$ as a function of modulus

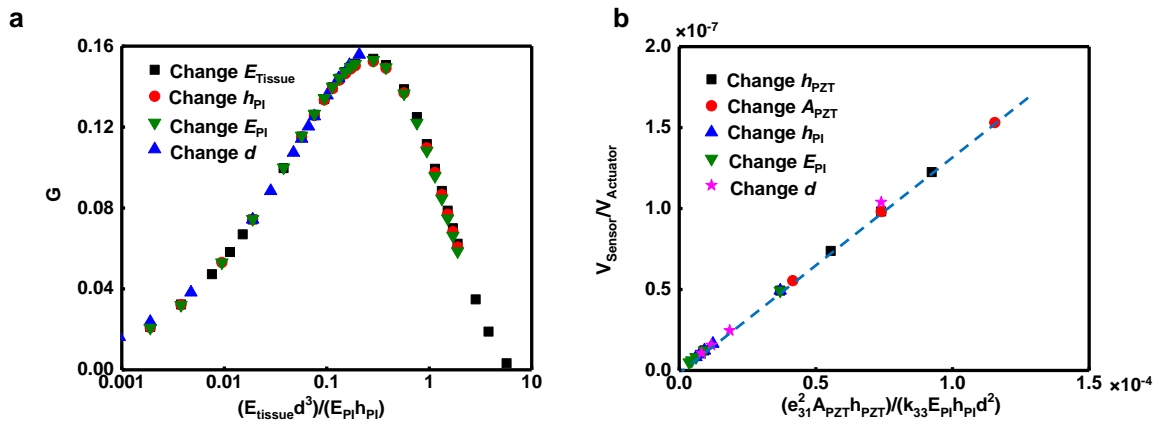


Figure S8. Validation of the scaling law. **a.** validate that the function G depends only on a single combination of parameters, $(E_{\text{Tissue}}d^3)/(E_{\text{PI}}h_{\text{PI}}^3)$. **b.** Validate the linear proportionality between the sensor voltage and $(A_{\text{PZT}}h_{\text{PZT}})/(E_{\text{PI}}h_{\text{PI}}d^2)$.

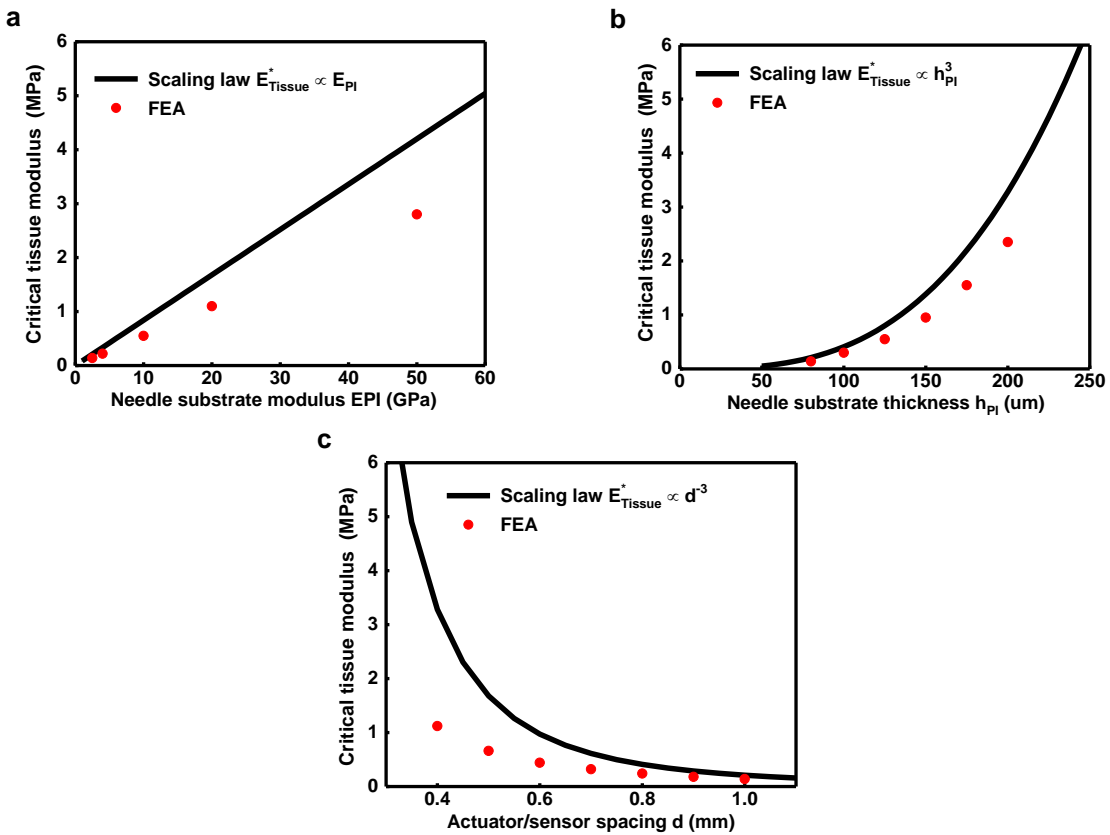


Figure S9. Prediction of the critical tissue modulus by the scaling law (black solid lines) and the FEA based on the geometrical dimensions of the device in the main text (red dots). **a.** influence of the needle substrate modulus. **b.** influence of the needle substrate thickness. **c.** influence of spacing between the actuator and the sensor.

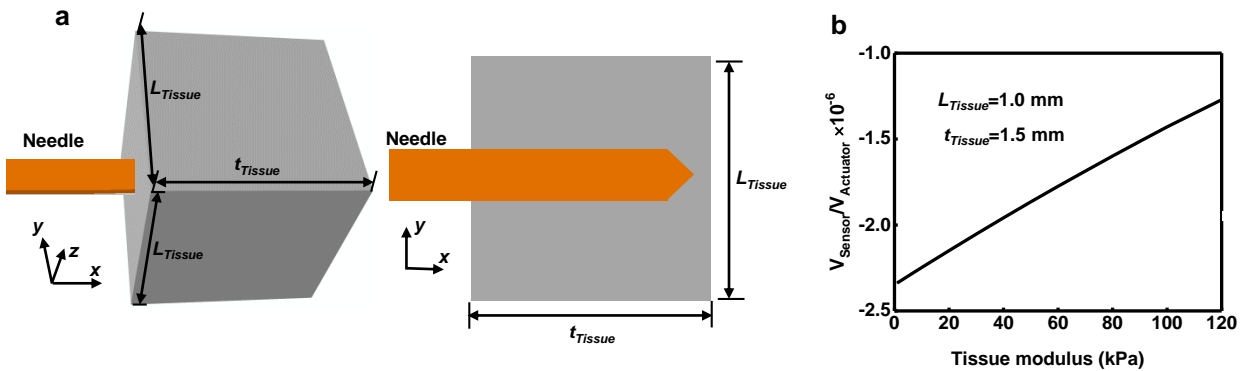


Figure S10. FEA prediction of the output voltage as a function of the tissue modulus for a small sample (size 1.0 mm \times 1.0 mm \times 1.5 mm)

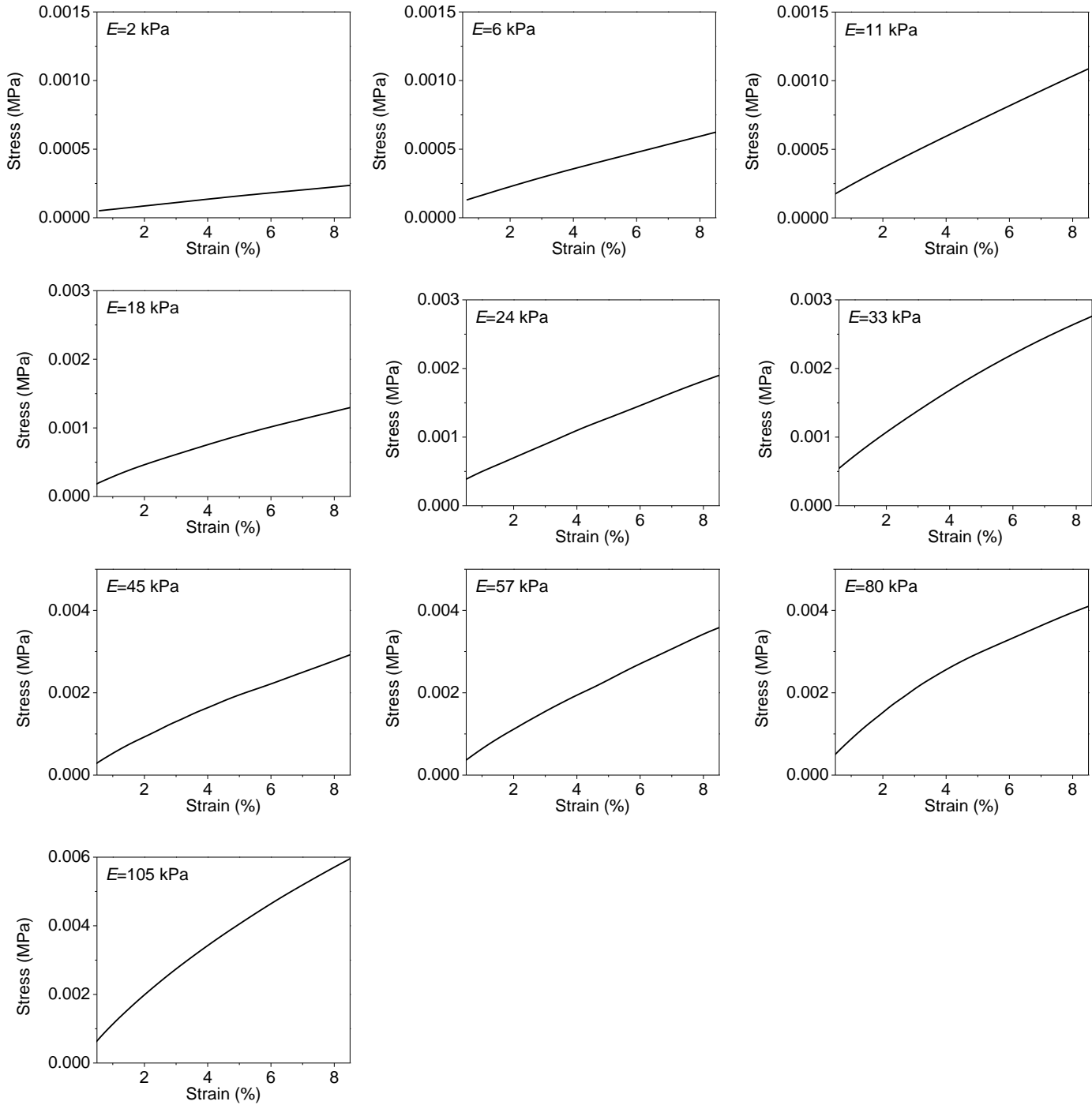


Figure S11. Tension stress-strain plots of artificial agarose gel in quasi-static strain rate regimes, with different modulus values.

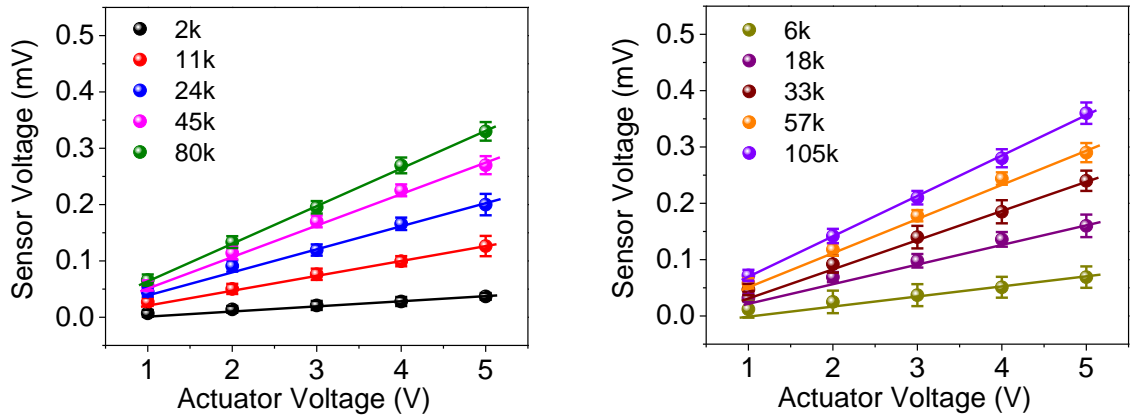


Figure S12. Experimental and theoretical analysis of the device operation. Voltage output of sensor as a function of actuator voltage, measured on ten different agarose gels with known moduli, separately evaluated by quasi-static dynamical mechanical analysis shown in Figure S10. Here, the symbols and lines correspond to experimental (E) and theoretical (T) results, respectively. Error bars correspond to calculated standard error deviation.

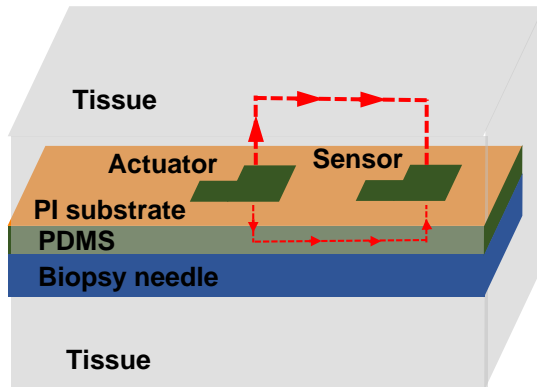


Figure S13. The mechanism of deformation for the modulus sensors integrated on a biopsy needle. The red arrows indicate that the deformation induced by the actuator is transferred to the sensor mainly via the deformation of the tissue and also the PDMS below the PI substrate

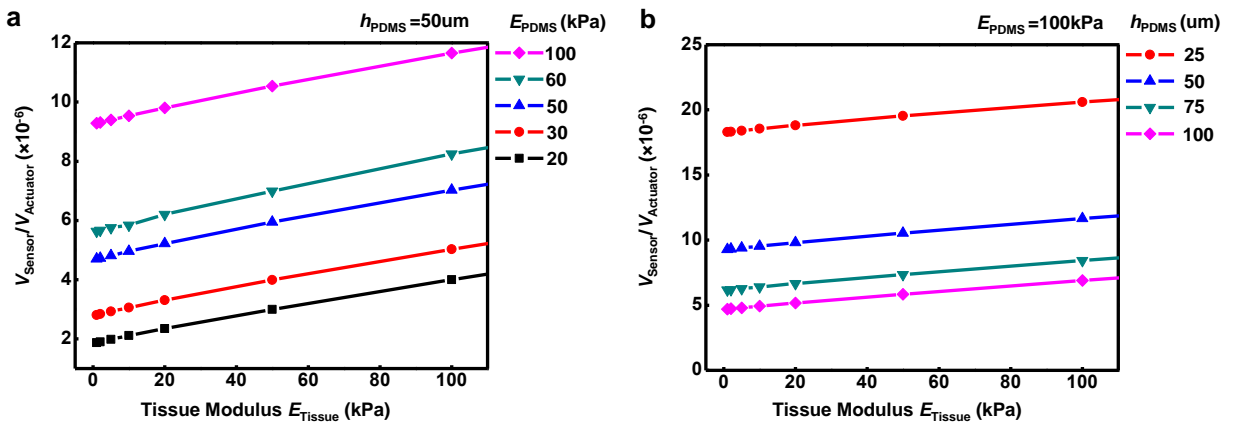


Figure S14. Theoretical analysis of biopsy needle based modulus sensor devices. a. Influence of the PDMS modulus on the sensor voltage. **b.** Influence of the PDMS thickness on the sensor voltage.

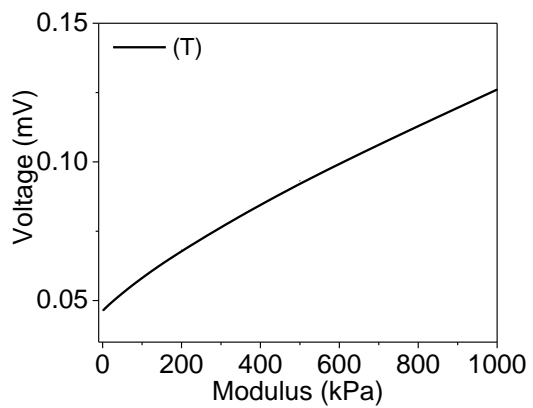


Figure S15. Theoretical analysis of V_{sensor} as a function of modulus, with actuator voltage of 5V

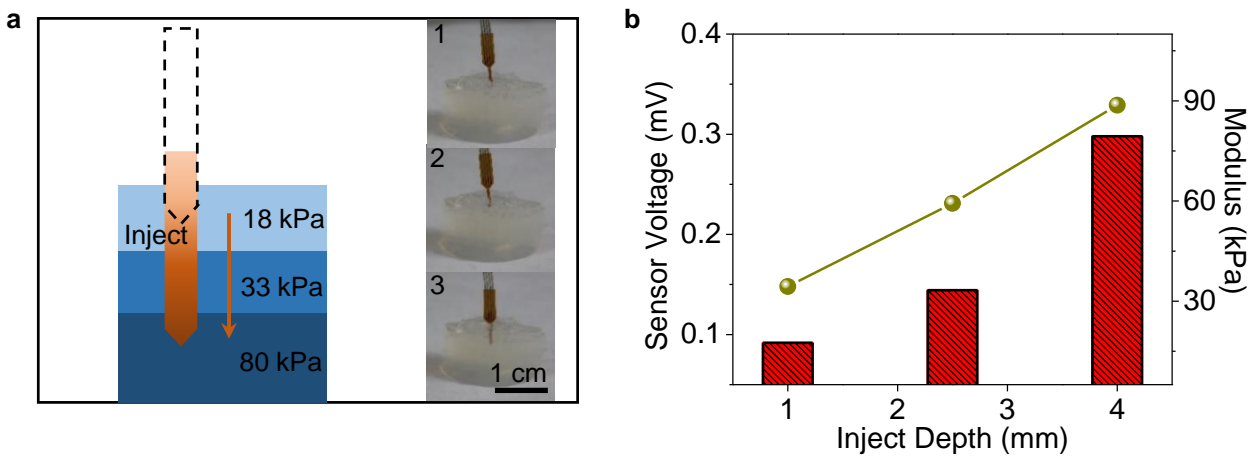


Figure S16. Experimental analysis and modulus measurements of multilayer artificial tissues. a. Modulus measurement on a multilayer sample, with three different modulus of 18, 33, and 80 kPa. **b.** Sensor voltage and modulus values at an actuation voltage of 5V, as a function of inject depth of the multilayer sample.

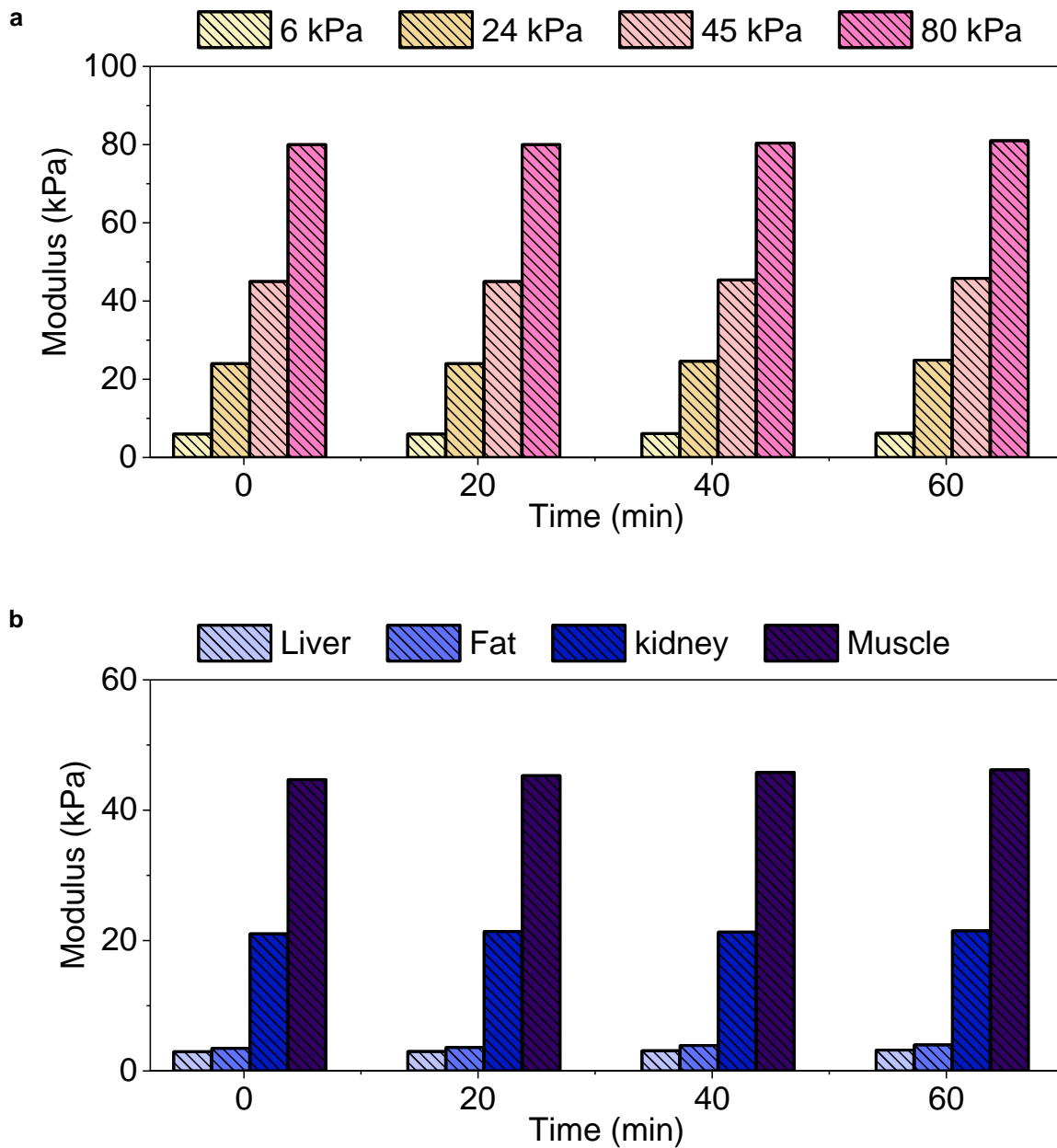


Figure S17. Modulus measurements modulus as function of time for 60 minutes. **a.** Measured on artificial agarose gel tissues with different modulus values. **b.** Measured on big tissues, including liver, fat, kidney, and muscle.

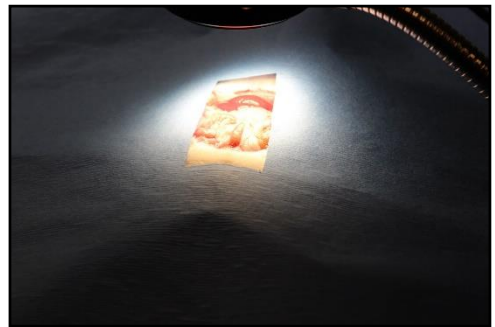


Figure S18. Illustration of surgical procedures for modulus measurement on the rat.

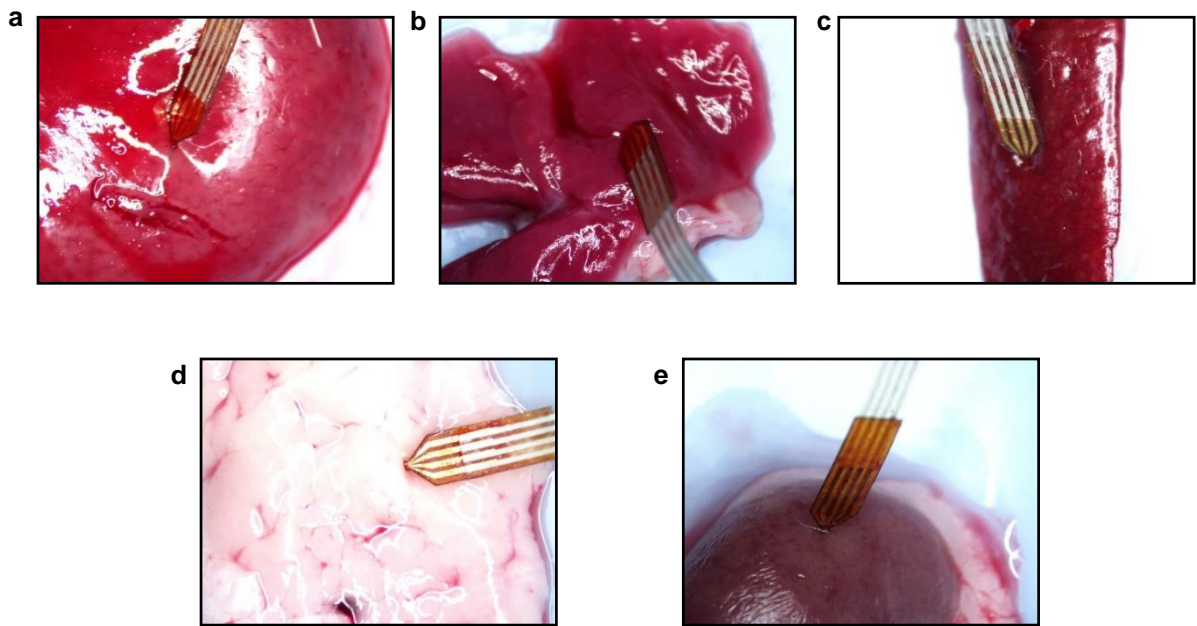


Figure S19. Ex-vivo measurement of organ tissues of the rat. Device insert and measure on liver, **a**, lung **b**, spleen **c**, fat **d**, and kidney **e**.

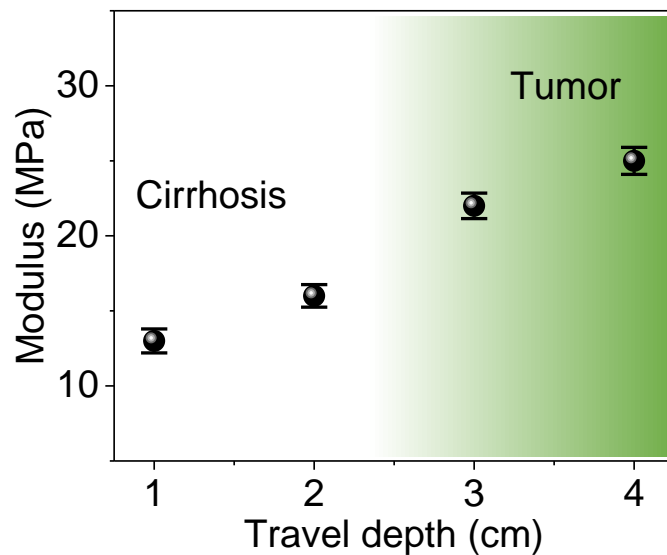


Figure S20. Real-time modulus measurement by a biopsy needle device. The device traverse from cirrhosis liver to tumor.

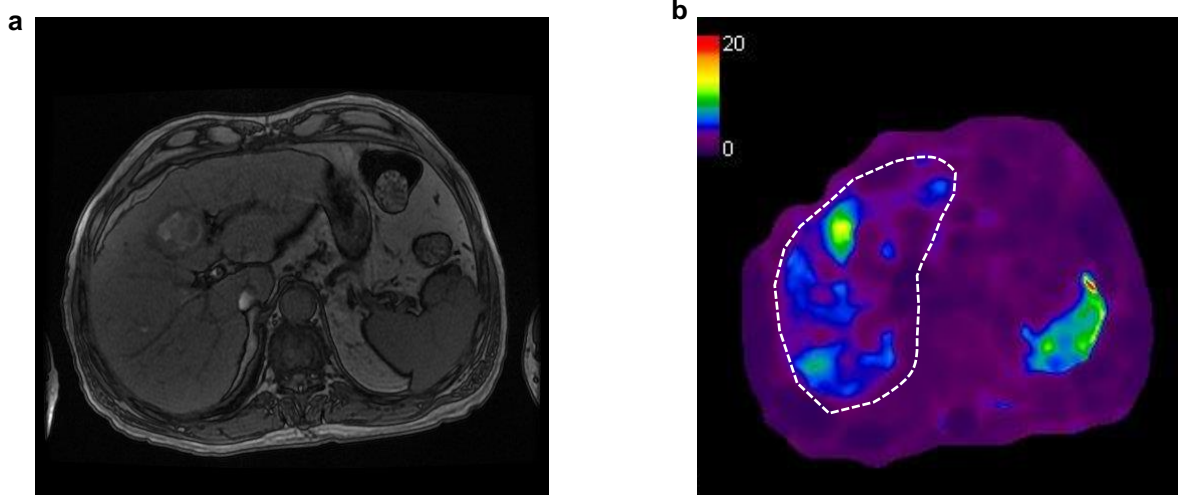


Figure S21. Images of a cirrhotic liver with hepatocellular carcinoma. **a.** Measured by Magnetic resonance image (MRI). **b.** Measured by Magnetic resonance elastography (MRE), shown stiffness mapping of the whole cross section of the patient.

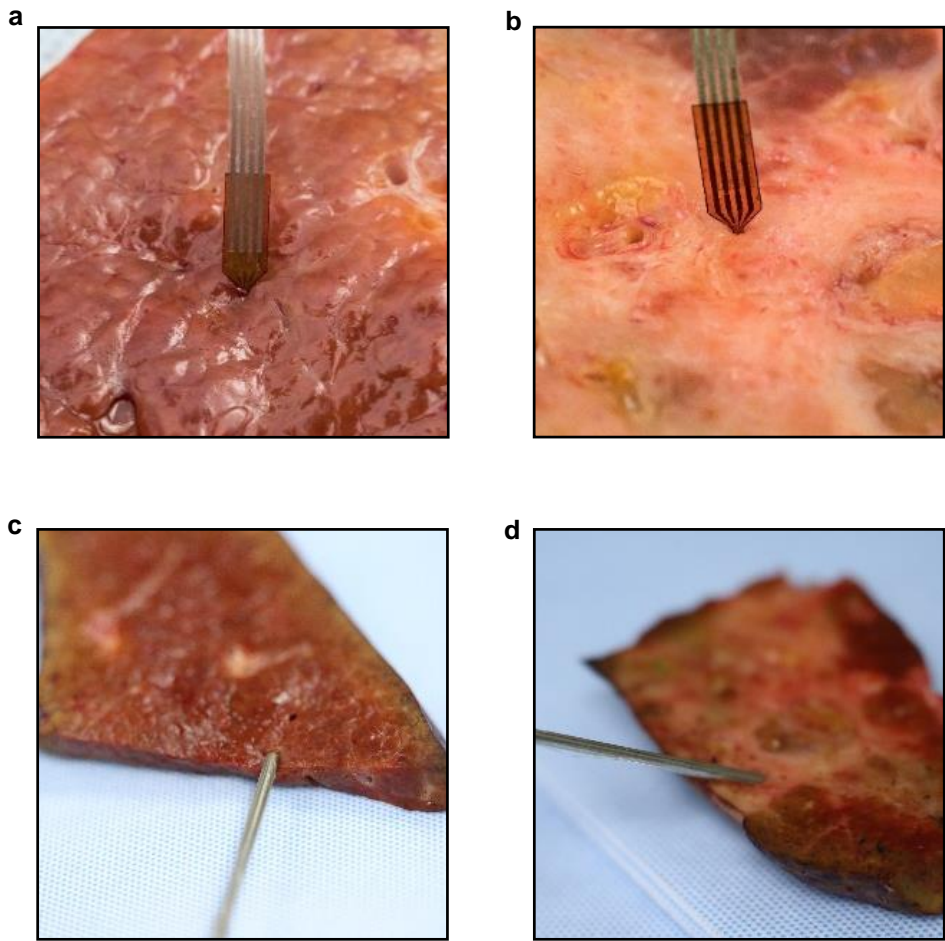


Figure S22. Image-guided modulus test. a,b, Photographs of a free standing device (device 1) injected into the non-tumor area of liver (a), and tumor (b). **c,d,** Photographs of a biopsy needle device (device 2) injected into the non-tumor area of liver (c), and tumor (d).